aerospace

MDPI

Article

An Aerodynamic Correction Technique for the Unsteady Subsonic Wing–Body Interference Model

Kun Mao [1,2,*], Wuxing Jing [1], Meihong Zhang [2] and Huining Zhang [2]

[1] Harbin Institute of Technology, Harbin 150006, China
[2] Shanghai Aircraft Design and Research Institute, Shanghai 200135, China
* Correspondence: maokunhao@126.com

Abstract: This paper investigates a novel correction technique for the unsteady subsonic wing–body interference model. The correction technique considers the unsteady forces on the lifting boxes and the body elements of an idealized aircraft model. The chosen simulation model was a passenger aircraft, and the transonic unsteady aerodynamics in sinusoidal pitch motion at four different frequencies are analyzed. The unsteady aerodynamics of the uncorrected DLM (doublet lattice method), ECFT (enhanced correction factor technique) and the new unsteady wing–body correction method are compared to the unsteady CFD simulation results. The results show that when the frequency is small, the new unsteady wing–body correction method can obtain certain benefits in terms of accuracy, for the lifting boxes and the body elements as well.

Keywords: correction technique; unsteady subsonic wing–body interference model; sinusoidal pitch motion; frequency

check for updates

Citation: Mao, K.; Jing, W.; Zhang, M.; Zhang, H. An Aerodynamic Correction Technique for the Unsteady Subsonic Wing–Body Interference Model. *Aerospace* **2023**, *10*, 837. https://doi.org/10.3390/aerospace10100837

Academic Editor: Zhichun Yang

Received: 25 August 2023
Revised: 20 September 2023
Accepted: 23 September 2023
Published: 26 September 2023

1. Introduction

With the improvement in aerodynamic and structural design technology, the structural flexibility of the modern large passenger aircraft has increased. Consequently, the frequency of elastic modes has decreased. This decrease brings the frequency of elastic modes close to the rigid-body flight dynamic modes, thereby affecting flight stability and controllability, and the design of control laws. Numerous studies have been undertaken looking at this problem [1–4]. However, the accuracy of the rigid-elastic coupling analysis mainly depends on the accuracy of the unsteady aerodynamic analysis.

The cruise speed of a large passenger aircraft is mainly in the high transonic range, where aerodynamics exhibit strong nonlinear characteristics. To calculate the unsteady nonlinear aerodynamic forces of elastic modes, the high-fidelity CFD (computational fluid dynamics) method is likely the most accurate simulation approach. An example of such a method is the unsteady aerodynamic analysis method based on the N–S (Navier–Stokes) equations [5,6]. However, due to the number of conditions considered during the flight dynamic analyses being significant, obtaining high-fidelity CFD solutions for each condition is impractical.

On the other hand, traditional unsteady linear aerodynamic analysis methods, which are suitable for low subsonic speed due to their extremely high efficiency, have been widely used since their development in the 1960s and 1970s [7,8]. Based on the principle of the inviscid and irrotational potential flow theory, the linear aerodynamic model forms lifting boxes, slender elements, and interference elements through the utilization of fundamental solutions like vortices and doublets. These methods are used to rapidly acquire unsteady linearized subsonic aerodynamic results. Such methods are extensively applied in commercial software, e.g., NASTRAN.

To achieve a balance between efficiency and accuracy of nonlinear aeroelastic analysis, researchers came up with some correction approaches for linear aerodynamic methods.

These correction methods are primarily focused on the diagonal correction method [9,10]. Moreno et al. [11] presented a full rank correction method based on the ECFT correction method [12]. Although this full rank correction method can take into account the influence of other modes to a certain extent, due to the fact that the coefficients on the diagonal still play a major role, the full rank correction method essentially behaves similarly to the diagonal correction method.

However, all the present correction methods for unsteady aerodynamics are only focused on the correction of lifting boxes. For the design of passenger aircraft, the current correction methods are insufficient. The reason is that lifting boxes are unable to accurately model the fuselage and nacelle component; also, it is necessary to take the wing–body interaction into account. Mao et al. [13] developed the ECFT method for the wing–body interference model. However, the ECFT method is only suitable for static aerodynamics, and not applicable to unsteady aerodynamics. This paper combines the characteristics of diagonal correction and ECFT correction, and then develops a technique for unsteady aerodynamic correction that works with models of wing–body interference. In the meantime, this technique is used to simulate a passenger aircraft in a transonic environment with sinusoidal pitching motion at various frequencies. The results are then compared with the high-fidelity CFD method to verify the accuracy at low frequency.

2. Materials and Methods

2.1. Unsteady Linear Aerodynamics for Wing–Body Interference Model

The lifting boxes, slender elements, and interference elements can be used to model the wing–body interference DLM model. Downwashes are presented as follows:

$$\left\{\begin{matrix} \underbrace{[w_w]}_{n_w\times 1} \\ \underbrace{[0]}_{(n_{tz}+n_{ty})\times 1} \\ \underbrace{[w_s]}_{(n_{tsz}+n_{tsy})\times 1} \end{matrix}\right\} = \underbrace{[AIC]}_{(n_w+n_{tz}+n_{ty}+n_{tsz}+n_{tsy})\times(n_w+n_{tz}+n_{ty}+n_{tsz}+n_{tsy})} \left\{\begin{matrix} \underbrace{[f'_w]}_{n_w\times 1} \\ \underbrace{[\mu_I]}_{(n_{tz}+n_{ty})\times 1} \\ \underbrace{[\mu_s]}_{(n_{tsz}+n_{tsy})\times 1} \end{matrix}\right\} \tag{1}$$

where:

w_w = downwashes for lifting boxes;
w_s = downwashes for slender elements;
f'_w = pressure coefficient along the lifting box;
μ_I = acceleration potential for interference element doublets;
μ_s = acceleration potential for slender element doublets;
$[AIC]$ = aerodynamic influence coefficients matrix related to the reduced frequency k, including real part $[AIC]_{\mathrm{REAL}}$ and imaginary part $[AIC]_{\mathrm{IMAG}}$;
n_w = number of lifting boxes;
n_{tz} or n_{ty} = number of interference elements in the z (vertical) or y (lateral) orientation;
n_{tsz} or n_{tsy} = number of slender elements in the z (vertical) or y (lateral) orientation.

The forces related to the singularities are shown as follows:

$$\left\{\begin{matrix} \underbrace{[P_w]}_{2n_w\times 1} \\ \underbrace{[P_s]}_{2(n_{tsy}+n_{tsz})\times 1} \end{matrix}\right\} = \bar{q} \underbrace{[SKJ]}_{2(n_w+n_{tsy}+n_{tsz})\times(n_w+n_{tz}+n_{ty}+n_{tsz}+n_{tsy})} \left\{\begin{matrix} \underbrace{[f'_w]}_{n_w\times 1} \\ \underbrace{[\mu_I]}_{(n_{tz}+n_{ty})\times 1} \\ \underbrace{[\mu_s]}_{(n_{tsz}+n_{tsy})\times 1} \end{matrix}\right\} \tag{2}$$

and the integration matrix $[SKJ]$ can be written as:

$$\underbrace{[SKJ]}_{2(n_w+n_{tsy}+n_{tsz})\times(n_w+n_{tz}+n_{ty}+n_{tsz}+n_{tsy})} = \begin{bmatrix} \underbrace{[S_{ww}]}_{2n_w\times n_w} & 0 & 0 \\ \underbrace{[S_{sw}]}_{2(n_{tsy}+n_{tsz})\times n_w} & \underbrace{[S_{sI}]}_{2(n_{tsy}+n_{tsz})\times(n_{tz}+n_{ty})} & \underbrace{[S_{ss}]}_{2(n_{tsy}+n_{tsz})\times(n_{tsz}+n_{tsy})} \end{bmatrix} \quad (3)$$

where:

P_w = lifting box force and moment;

P_s = slender element force and moment;

$[SKJ]$ = integration matrix;

S_{ww} = lifting box element area for forces and lifting box element area times quarter chord length for moments;

$\begin{bmatrix} S_{sw} & S_{sI} & S_{ss} \end{bmatrix}$ = integration matrix for slender elements related to the reduced frequency k, including real part $\begin{bmatrix} S_{swREAL} & S_{sIREAL} & S_{ssREAL} \end{bmatrix}$ and imaginary part $\begin{bmatrix} S_{swIMAG} & S_{sIIMAG} & S_{ssIMAG} \end{bmatrix}$, and the rows for the moment are all zero.

If we extract the matrix rows containing force and moment from Equation (2), Equations (4) and (5) below show the expression in which F stands for force and M represents moment.

$$\left\{ \begin{array}{c} \underbrace{[F_w]}_{n_w\times 1} \\ \underbrace{[F_s]}_{(n_{tsy}+n_{tsz})\times 1} \end{array} \right\} = \overline{q} \underbrace{[SKJ]_F}_{(n_w+n_{tsy}+n_{tsz})\times(n_w+n_{tz}+n_{ty}+n_{tsz}+n_{tsy})} \left\{ \begin{array}{c} \underbrace{[f'_w]}_{n_w\times 1} \\ \underbrace{[\mu_I]}_{(n_{tz}+n_{ty})\times 1} \\ \underbrace{[\mu_s]}_{(n_{tsz}+n_{tsy})\times 1} \end{array} \right\} \quad (4)$$

$$\left\{ \begin{array}{c} \underbrace{[M_w]}_{n_w\times 1} \\ \underbrace{[M_s]}_{(n_{tsy}+n_{tsz})\times 1} \end{array} \right\} = \overline{q} \underbrace{[SKJ]_M}_{(n_w+n_{tsy}+n_{tsz})\times(n_w+n_{tz}+n_{ty}+n_{tsz}+n_{tsy})} \left\{ \begin{array}{c} \underbrace{[f'_w]}_{n_w\times 1} \\ \underbrace{[\mu_I]}_{(n_{tz}+n_{ty})\times 1} \\ \underbrace{[\mu_s]}_{(n_{tsz}+n_{tsy})\times 1} \end{array} \right\} \quad (5)$$

2.2. A Correction Method for Wing–Body Interference Model to Correct Unsteady [AIC] matrix

The correction technique uses the steady aerodynamics at $k = 0$ to construct a correction matrix and correct the unsteady $[AIC]$ matrix at $k \neq 0$.

The correction technique starts with defining the steady downwashes w_0 at $k = 0$ for the linear wing–body interference model, shown as follows:

$$\underbrace{[w_0]}_{(n_w+n_{tz}+n_{ty}+n_{tsz}+n_{tsy})\times 1} = \left\{ \begin{array}{c} \underbrace{[w_{0w}]}_{n_w\times 1} \\ \underbrace{[0]}_{(n_{tz}+n_{ty})\times 1} \\ \underbrace{[w_{0s}]}_{(n_{tsz}+n_{tsy})\times 1} \end{array} \right\} \quad (6)$$

The pressure coefficient (f'_w) of the lifting boxes, the acceleration potential of the interference elements (μ_I) and slender elements (μ_s) for the steady linear wing–body interference model can be obtained from Equation (1):

$$\left\{\begin{array}{c}\underbrace{[f'_{0w}]}_{n_w\times 1}\\ \underbrace{[\mu_{0I}]}_{(n_{tz}+n_{ty})\times 1}\\ \underbrace{[\mu_{0s}]}_{(n_{tsz}+n_{tsy})\times 1}\end{array}\right\} = \underbrace{[AIC]_{k=0}^{-1}}_{(n_w+n_{tz}+n_{ty}+n_{tsz}+n_{tsy})\times(n_w+n_{tz}+n_{ty}+n_{tsz}+n_{tsy})} \cdot \underbrace{[w_0]}_{(n_w+n_{tz}+n_{ty}+n_{tsz}+n_{tsy})\times 1} \tag{7}$$

To generate the correction matrix, a set of lifting forces obtained from steady experiments or CFD simulations needs to be mapped onto the lifting boxes and slender elements. The aerodynamic forces after mapping are shown as follows:

$$\underbrace{[F_1]}_{(n_w+n_{tsy}+n_{tsz})\times 1} = \left\{\begin{array}{c}\underbrace{[F_{1w}]}_{n_w\times 1}\\ \underbrace{[F_{1s}]}_{(n_{tsy}+n_{tsz})\times 1}\end{array}\right\} \tag{8}$$

To obtain the appropriate $\left[f'_{1w} \quad \mu_{1I} \quad \mu_{1s}\right]^T$ related to Equation (8), several assumptions have to be made, since the integration matrix $[SKJ]_F$ in Equation (4) is an unfilled row:

Assumption 1. *the number of interference elements and the slender elements are the same, which means $n_{tsy} = n_{ty}$ and $n_{tsz} = n_{tz}$;*

Assumption 2. *the proportion of μ_{1s}/μ_{1I} is equal to the μ_{0s}/μ_{0I}.*

Suggest the proportion of μ_{0s}/μ_{0I} is σ_{si}, Equation (4) at $k = 0$ can then be rewritten as follows:

$$\left\{\begin{array}{c}\underbrace{[F_{1w}]}_{n_w\times 1}\\ \underbrace{[F_{1s}]}_{(n_{tsy}+n_{tsz})\times 1}\end{array}\right\} = \bar{q}\left[\begin{array}{cc}\underbrace{[S_{ww}]_F}_{n_w\times n_w} & 0\\ \underbrace{[S_{sw}]_F}_{(n_{tsy}+n_{tsz})\times n_w} & \underbrace{[S_{sI}]_F+\sigma_{si}[S_{ss}]_F}_{(n_{tsy}+n_{tsz})\times(n_{tsz}+n_{tsy})}\end{array}\right]_{k=0}\left\{\begin{array}{c}\underbrace{[f'_{1w}]}_{n_w\times 1}\\ \underbrace{[\mu_{1I}]}_{(n_{tsz}+n_{tsy})\times 1}\end{array}\right\} = \bar{q}\left([SKJ]'_F\right)_{k=0}\left\{\begin{array}{c}\underbrace{[f'_{1w}]}_{n_w\times 1}\\ \underbrace{[\mu_{1I}]}_{(n_{tsz}+n_{tsy})\times 1}\end{array}\right\} \tag{9}$$

where $[SKJ]'_F$ is with a filled row, and:

$$\left\{\begin{array}{c}\underbrace{[f'_{1w}]}_{n_w\times 1}\\ \underbrace{[\mu_{1I}]}_{(n_{tsz}+n_{tsy})\times 1}\end{array}\right\} = \frac{1}{\bar{q}}\left([SKJ]'_F\right)_{k=0}^{-1}\left\{\begin{array}{c}\underbrace{[F_{1w}]}_{n_w\times 1}\\ \underbrace{[F_{1s}]}_{(n_{tsy}+n_{tsz})\times 1}\end{array}\right\},\ \underbrace{[\mu_{1s}]}_{(n_{tsz}+n_{tsy})\times 1} = \sigma_{si}\cdot\underbrace{[\mu_{1I}]}_{(n_{tsz}+n_{tsy})\times 1} \tag{10}$$

Hence:

$$\underbrace{[f'_1]_{k=0}}_{(n_w+2n_{tsz}+2n_{tsy})\times 1} = \left\{\begin{array}{c}\underbrace{[f'_{1w}]}_{n_w\times 1}\\ \underbrace{[\mu_{1I}]}_{(n_{tsz}+n_{tsy})\times 1}\\ \underbrace{[\mu_{1s}]}_{(n_{tsz}+n_{tsy})\times 1}\end{array}\right\} \tag{11}$$

For the diagonal correction method, the correction matrix $[WJJ]$ is assumed as a diagonal matrix, and can be calculated as follows:

$$\underbrace{\begin{bmatrix} W_{jj} & 0 \\ 0 & \dots \end{bmatrix}}_{(n_w+2n_{tsz}+2n_{tsy})\times(n_w+2n_{tsz}+2n_{tsy})} \cdot \underbrace{[AIC]_{k=0}^{-1}}_{(n_w+2n_{tsz}+2n_{tsy})\times(n_w+2n_{tsz}+2n_{tsy})} \cdot \underbrace{[w_0]}_{(n_w+2n_{tsz}+2n_{tsy})\times 1} = \underbrace{[f_1']_{k=0}}_{(n_w+2n_{tsz}+2n_{tsy})\times 1} \tag{12}$$

For the ECFT correction method, $[w_0]$ and $[f_1']$ should be converted to the complimentary null subspace:

$$\underbrace{[\Omega_0]}_{(n_w+2n_{tsz}+2n_{tsy})\times(n_w+2n_{tsz}+2n_{tsy})} = \left[\underbrace{[w_0]}_{(n_w+2n_{tsz}+2n_{tsy})\times 1} \vdots \underbrace{[null(w_0)]}_{(n_w+2n_{tsz}+2n_{tsy})\times(n_w+2n_{tsz}+2n_{tsy}-1)} \right] \tag{13}$$

$$\underbrace{[F_1']}_{(n_w+2n_{tsz}+2n_{tsy})\times(n_w+2n_{tsz}+2n_{tsy})} = \left[\underbrace{[f_1']_{k=0}}_{(n_w+2n_{tsz}+2n_{tsy})\times 1} \vdots \underbrace{[AIC]^{-1}\cdot[null(w_0)]}_{(n_w+2n_{tsz}+2n_{tsy})\times(n_w+2n_{tsz}+2n_{tsy}-1)} \right] \tag{14}$$

Hence $[WJJ]$ can be obtained by:

$$\underbrace{[WJJ]}_{(n_w+2n_{tsz}+2n_{tsy})\times(n_w+2n_{tsz}+2n_{tsy})} \cdot \underbrace{[AIC]_{k=0}^{-1}}_{(n_w+2n_{tsz}+2n_{tsy})\times(n_w+2n_{tsz}+2n_{tsy})} \cdot \underbrace{[\Omega_0]}_{(n_w+2n_{tsz}+2n_{tsy})\times(n_w+2n_{tsz}+2n_{tsy})} = \underbrace{[F_1']}_{(n_w+2n_{tsz}+2n_{tsy})\times(n_w+2n_{tsz}+2n_{tsy})} \tag{15}$$

For the unsteady situation, when the reduced frequency $k = k_i \neq 0$, both the diagonal correction method in Equation (12) and the ECFT correction method in Equation (15) will encounter some problems.

When $k = k_i \neq 0$, the unsteady downwashes w, unsteady $[AIC]$ matrix, and body element part of integration matrix $[SKJ]_F$ will have two parts: a real one (subscript REAL) and an imaginary one (subscript IMAG). Hence the pressure coefficient (f_w') of the lifting boxes, the acceleration potential of the interference elements (μ_I) and the slender elements (μ_s) due to unsteady downwashes for the linear wing–body interference model are:

$$\left(\left\{ \begin{array}{c} \underbrace{[f_w']}_{n_w\times 1} \\ \underbrace{[\mu_I]}_{(n_{tz}+n_{ty})\times 1} \\ \underbrace{[\mu_s]}_{(n_{tsz}+n_{tsy})\times 1} \end{array} \right\}_{REAL} + \left\{ \begin{array}{c} \underbrace{[f_w']}_{n_w\times 1} \\ \underbrace{[\mu_I]}_{(n_{tz}+n_{ty})\times 1} \\ \underbrace{[\mu_s]}_{(n_{tsz}+n_{tsy})\times 1} \end{array} \right\}_{IMAG} \right) = \underbrace{\left([AIC]_{REAL_i}^{-1} + [AIC]_{IMAG}^{-1}\right)}_{(n_w+n_{tz}+n_{ty}+n_{tsz}+n_{tsy})\times(n_w+n_{tz}+n_{ty}+n_{tsz}+n_{tsy})} \cdot \underbrace{([w]_{REAL} + [w]_{IMAG})}_{(n_w+n_{tz}+n_{ty}+n_{tsz}+n_{tsy})\times 1} \tag{16}$$

where the proportion of the imaginary part $(\mu_s/\mu_I)_{IMAG}$ is not equal to $(\mu_s/\mu_I)_{k=0}$, which means the process in Equation (9) is no longer suitable for the imaginary part. In fact, the $(\mu_s/\mu_I)_{IMAG}$ will vary for different reduced frequency k, making it difficult to find this proportion. This variability makes the diagonal correction method not suitable for the imaginary part of the body elements.

For the ECFT correction method, Equation (13) to Equation (15) show an obvious problem for any downwash in the null subspace matrix, as the aerodynamic force output would be exactly the same as the uncorrected DLM. Consequently, the imaginary downwashes $[w]_{IMAG}$ remain uncorrected.

The correction method to correct the unsteady $[AIC]$ matrix of the wing–body interference model is proposed under the following preconditions:

1. The reduced frequency k is small; therefore, the real part of the unsteady downwashes w, unsteady $[AIC]$ matrix, and integration matrix $[SKJ]$ will be close to $k = 0$;
2. Fortunately, when the reduced frequency k is small, the imaginary part of the uncorrected aerodynamic force for body elements is small, and close to the target aerodynamic force.

The basic correction ideas are:

1. The real part of the wing–body interference model and the imaginary part of the lifting surface can be corrected by using the diagonal correction method, while the imaginary part of the body elements can be left uncorrected;
2. A unified correction matrix is required to simultaneously correct the real and imaginary parts for all elements in the wing–body interference model.

To achieve this idea, Equation (14) can be changed to:

$$\underbrace{[F_1']_{unsteady-wb}}_{(n_w+2n_{tsz}+2n_{tsy})\times(n_w+2n_{tsz}+2n_{tsy})} = \left[\begin{array}{ccc} \underbrace{[f_1']_{k=0}}_{(n_w+2n_{tsz}+2n_{tsy})\times 1} & \vdots & \begin{array}{c}\underbrace{W_{jj}\cdot[AIC]^{-1}\cdot[null(w_0)]}_{n_w\times(n_w+2n_{tsz}+2n_{tsy}-1)} \\ \underbrace{[AIC]^{-1}\cdot[null(w_0)]}_{(2n_{tsz}+2n_{tsy})\times(n_w+2n_{tsz}+2n_{tsy}-1)}\end{array} \end{array}\right] \quad (17)$$

where W_{jj} can be acquired from Equation (12). By substituting Equation (17) into Equation (15), the correction matrix [*WJJ*] to correct unsteady [*AIC*] for the wing–body interference model is derived.

2.3. A Correction Method for Wing–Body Interference Model to Correct Unsteady Force and Moment

The [*WJJ*] matrix can be calculated by the process outlined above, and it can be directly used to correct the [*AIC*] matrix. However, in some circumstances, such as when it is used as an input to MSC.NASTRAN, the [*WKK*] matrix might be required to correct the force and moment matrix. The differences between using the [*WJJ*] and [*WKK*] matrix to generate the DLM forces and moments are shown as follows:

$$\left\{\begin{array}{c}\underbrace{[P_w]}_{2n_w\times 1} \\ \underbrace{[P_s]}_{2(n_{tsy}+n_{tsz})\times 1}\end{array}\right\} = \bar{q}\underbrace{[SKJ]}_{2(n_w+n_{tsy}+n_{tsz})\times(n_w+2n_{tsz}+2n_{tsy})}\cdot\underbrace{[WJJ]}_{(n_w+2n_{tsz}+2n_{tsy})\times(n_w+2n_{tsz}+2n_{tsy})}\left\{\begin{array}{c}\underbrace{[f_{0w}']}_{n_w\times n_m} \\ \underbrace{[\mu_{0I}]}_{(n_{tz}+n_{ty})\times n_m} \\ \underbrace{[\mu_{0s}]}_{(n_{tsz}+n_{tsy})\times n_m}\end{array}\right\} \quad (18)$$

$$\left\{\begin{array}{c}\underbrace{[P_w]}_{2n_w\times 1} \\ \underbrace{[P_s]}_{2(n_{tsy}+n_{tsz})\times 1}\end{array}\right\} = \bar{q}\underbrace{[WKK]}_{2(n_w+n_{tsy}+n_{tsz})\times 2(n_w+n_{tsy}+n_{tsz})}\cdot\underbrace{[SKJ]}_{2(n_w+n_{tsy}+n_{tsz})\times(n_w+2n_{tsz}+2n_{tsy})}\left\{\begin{array}{c}\underbrace{[f_{0w}']}_{n_w\times n_m} \\ \underbrace{[\mu_{0I}]}_{(n_{tz}+n_{ty})\times n_m} \\ \underbrace{[\mu_{0s}]}_{(n_{tsz}+n_{tsy})\times n_m}\end{array}\right\} \quad (19)$$

Equations (18) and (19) should be equal to each other, which means:

$$\underbrace{[WKK]}_{2(n_w+n_{tsy}+n_{tsz})\times 2(n_w+n_{tsy}+n_{tsz})}\cdot\underbrace{[SKJ]}_{2(n_w+n_{tsy}+n_{tsz})\times(n_w+2n_{tsz}+2n_{tsy})} = \underbrace{[SKJ]}_{2(n_w+n_{tsy}+n_{tsz})\times(n_w+2n_{tsz}+2n_{tsy})}\cdot\underbrace{[WJJ]}_{(n_w+2n_{tsz}+2n_{tsy})\times(n_w+2n_{tsz}+2n_{tsy})} \quad (20)$$

The [*WKK*] matrix and [*SKJ*] matrix are divided into force and moment components, and Equation (20) can be transferred into the following forms:

$$\underbrace{[WKK]_F}_{(n_w+n_{tsy}+n_{tsz})\times(n_w+n_{tsy}+n_{tsz})}\cdot\underbrace{[SKJ]_F}_{(n_w+n_{tsy}+n_{tsz})\times(n_w+2n_{tsz}+2n_{tsy})} = \underbrace{([SKJ]\cdot[WJJ])_F}_{(n_w+n_{tsy}+n_{tsz})\times(n_w+2n_{tsz}+2n_{tsy})} \quad (21)$$

$$\underbrace{[WKK]_M}_{(n_w+n_{tsy}+n_{tsz})\times(n_w+n_{tsy}+n_{tsz})} \cdot \underbrace{[SKJ]_M}_{(n_w+n_{tsy}+n_{tsz})\times(n_w+2n_{tsz}+2n_{tsy})} = \underbrace{([SKJ]\cdot[WJJ])_M}_{(n_w+n_{tsy}+n_{tsz})\times(n_w+2n_{tsz}+2n_{tsy})} \tag{22}$$

In Equations (21) and (22), for the wing–body interference model, $[SKJ]_F$ and $[SKJ]_M$ all have unfilled rows. To solve these equations, Assumption 2 mentioned earlier has been applied here, and a new $[SKJ]_{F_{new}}$ and $([SKJ]\cdot[WJJ])_{F_{new}}$ can be obtained, shown as follows:

$$\underbrace{[SKJ]_{F_{new}}}_{(n_w+n_{tsy}+n_{tsz})\times(n_w+n_{tsz}+n_{tsy})} = \left[\underbrace{[SKJ]_F}_{(n_w+n_{tsy}+n_{tsz})\times n_w} \vdots \underbrace{[SKJ]_F}_{(n_w+n_{tsy}+n_{tsz})\times((n_w+1):(n_w+n_{tsy}+n_{tsz}))} + \sigma_{si}\cdot \underbrace{[SKJ]_F}_{(n_w+n_{tsy}+n_{tsz})\times((n_w+n_{tsy}+n_{tsz}+1):(n_w+2n_{tsy}+2n_{tsz}))} \right] \tag{23}$$

$$\underbrace{([SKJ]\cdot[WJJ])_{F_{new}}}_{(n_w+n_{tsy}+n_{tsz})\times(n_w+n_{tsz}+n_{tsy})} = \left[\underbrace{([SKJ]\cdot[WJJ])_F}_{(n_w+n_{tsy}+n_{tsz})\times(n_w)} \vdots \underbrace{([SKJ]\cdot[WJJ])_F}_{(n_w+n_{tsy}+n_{tsz})\times((n_w+1):(n_w+n_{tsy}+n_{tsz}))} + \sigma_{si}\cdot \underbrace{([SKJ]\cdot[WJJ])_F}_{(n_w+n_{tsy}+n_{tsz})\times((n_w+n_{tsy}+n_{tsz}+1):(n_w+2n_{tsy}+2n_{tsz}))} \right] \tag{24}$$

To eliminate the zero rows of the slender elements in the matrix $[SKJ]_M$, a small number ε was introduced, and the aerodynamic center lies $\varepsilon\cdot l$ behind the midpoint, where l is the length of the slender element. Hence $[SKJ]_{M_{new}}$ and $([SKJ]\cdot[WJJ])_{M_{new}}$ can be calculated as follows:

$$\underbrace{[SKJ]_{M_{new}}}_{(n_w+n_{tsy}+n_{tsz})\times(n_w+n_{tsz}+n_{tsy})} = \left[\underbrace{[SKJ]_M}_{(n_w+n_{tsy}+n_{tsz})\times n_w} \vdots \underbrace{[SKJ]_M}_{(n_w+n_{tsy}+n_{tsz})\times((n_w+1):(n_w+n_{tsy}+n_{tsz}))} + \sigma_{si}\cdot \underbrace{[SKJ]_M}_{(n_w+n_{tsy}+n_{tsz})\times((n_w+n_{tsy}+n_{tsz}+1):(n_w+2n_{tsy}+2n_{tsz}))} \right] \tag{25}$$

$$\underbrace{([SKJ]\cdot[WJJ])_{M_{new}}}_{(n_w+n_{tsy}+n_{tsz})\times(n_w+n_{tsz}+n_{tsy})} = \left[\underbrace{([SKJ]\cdot[WJJ])_M}_{(n_w+n_{tsy}+n_{tsz})\times(n_w)} \vdots \underbrace{([SKJ]\cdot[WJJ])_M}_{(n_w+n_{tsy}+n_{tsz})\times((n_w+1):(n_w+n_{tsy}+n_{tsz}))} + \sigma_{si}\cdot \underbrace{([SKJ]\cdot[WJJ])_M}_{(n_w+n_{tsy}+n_{tsz})\times((n_w+n_{tsy}+n_{tsz}+1):(n_w+2n_{tsy}+2n_{tsz}))} \right] \tag{26}$$

By replacing $[SKJ]_F$, $[SKJ]_M$, $([SKJ]\cdot[WJJ])_F$, and $([SKJ]\cdot[WJJ])_M$ in Equations (21) and (22) with $[SKJ]_{F_{new}}$, $[SKJ]_{M_{new}}$, $([SKJ]\cdot[WJJ])_{F_{new}}$, and $([SKJ]\cdot[WJJ])_{M_{new}}$, $[WKK]_F$ and $[WKK]_M$ can be acquired and constructed into the final $[WKK]$.

2.4. Simulation Model

The chosen simulation model is presented in Figure 1: the aircraft is a conventional wing-mounted and low-horizontal-tail configuration. The wing, horizontal tail, vertical tail, fuselage, nacelle, and pylon are included in the aircraft model. The wing span and the fuselage length of this aircraft are shown in Table 1.

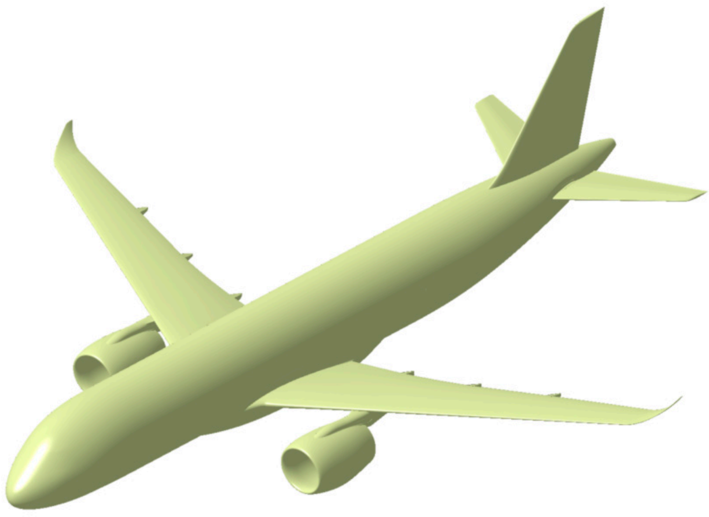

Figure 1. Illustration of the chosen passenger aircraft model configuration used for simulations.

Table 1. Main parameters of the aircraft model.

	Wing Span, m	Horizontal Tail Span, m	Fuselage Length, m	Height, m
Simulation model	≈35	≈13	≈39	≈12

Figure 2 presents the wing–body interference DLM model. Those parts modelled as lifting boxes were the wing, horizontal tail, vertical tail, and pylon. The fuselage and nacelle, on the other hand, were modeled as body elements, including slender elements and interference elements. In contrast to the interference elements, the width of the slender elements varied from front to back. Each interference element and slender element was oriented in both the z (vertical) and y (lateral) orientations. In Table 2, the number of elements is displayed. The simulation software decided on was MSC.NASTRAN.

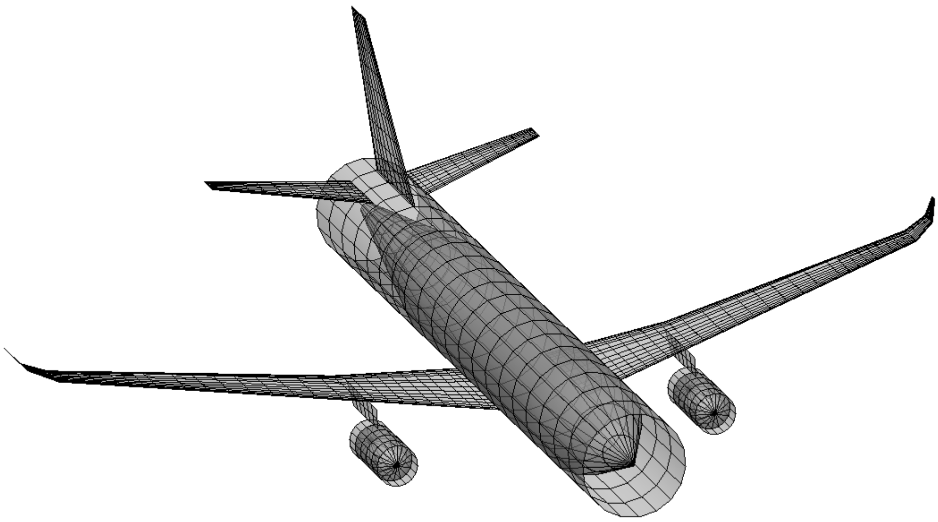

Figure 2. The wing–body interference DLM model.

Table 2. Number of elements for the wing–body interference DLM model.

Name of Elements	Number
Total Elements	1817
Lifting Boxes	1757
Slender Elements	30
Interference Elements	30

The linear DLM model needs to be corrected by the steady CFD results. Additionally, unsteady CFD was conducted for verification purposes. CFD++ was selected as the CFD solver for both steady and unsteady CFD analysis, utilizing Menter's k-Omega SST model [14]. The aircraft CFD surface mesh is shown in Figure 3 and the grid parameters are presented in Table 3.

To verify the accuracy of the correction method, the unsteady motion is assumed to be the sinusoidal pitch motion, with the center of gravity as the reference point for the pitch motion. There are two advantages to choosing pitch motion for validation:

1. Pitch motion is a very typical flight motion;
2. The wing is close to the reference point, while the tail is far away from it. The different sections of the fuselage range differently to the reference point. The varying distances result in the downwashes w of the real and imaginary parts occupying different proportions in different components during pitch motion.

Figure 3. CFD surface mesh.

Table 3. CFD grid details.

Name of Parameters	Parameter
Total no. of points/[10^6]	29.2
Total no. of cells/[10^6]	28.9
First wall-normal layer spacing/[µm]	10
Expansion ratio	1.2
No. of wall-normal layers	40

Corresponding to the pitch motion, the deflection shape for steady CFD results to correct the linear DLM model is the angle of attack.

3. Results

3.1. Pressure Difference Distribution Comparison at 1 HZ

The transonic Mach number and the Reynolds number applied to the steady CFD and unsteady CFD simulation cases are the same. For the steady CFD simulations, two angles of attack, $\alpha = 0^\circ$ and $\alpha = 1^\circ$, were examined to construct the aerodynamic force for a unit angle of attack. For unsteady CFD simulations, motions are a small sinusoidal oscillation with an initial position of $\alpha = 0^\circ$ and relative to the center of gravity. This configuration was designed to ensure that there was no flow separation during the oscillation. The frequencies of oscillation were set at 1 HZ, 5 HZ, 10 HZ and 20 HZ.

The pressure difference distributions caused by oscillation at a unit angle of attack at 1 HZ, as generated from several correction techniques, are compared with the unsteady CFD results. The comparisons of the results are presented in Figures 4–7. Six streamwise wing sections were chosen along the spanwise direction for the wing component, and four sections were chosen for the horizontal tail. Eta shown in the figures represents the position of the wing section relative to the symmetry plane in a spanwise direction.

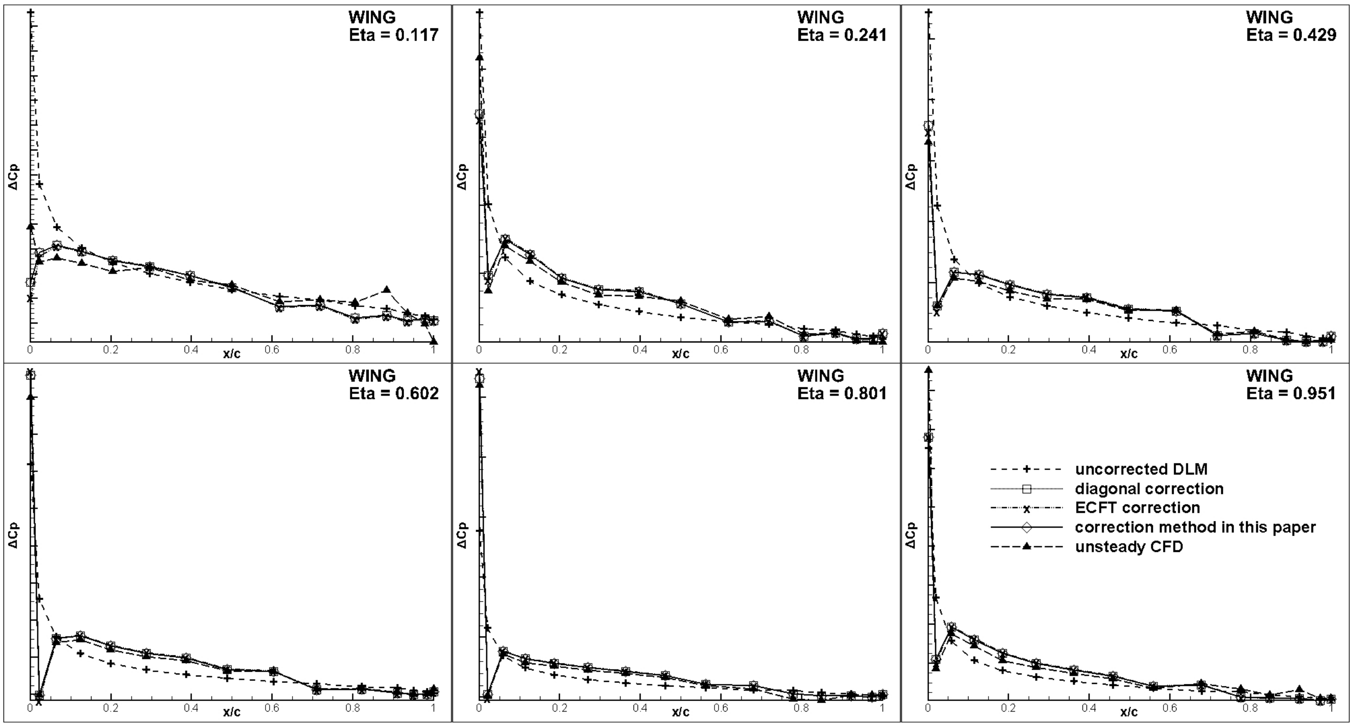

Figure 4. Real ΔCp of wing component at 1 HZ.

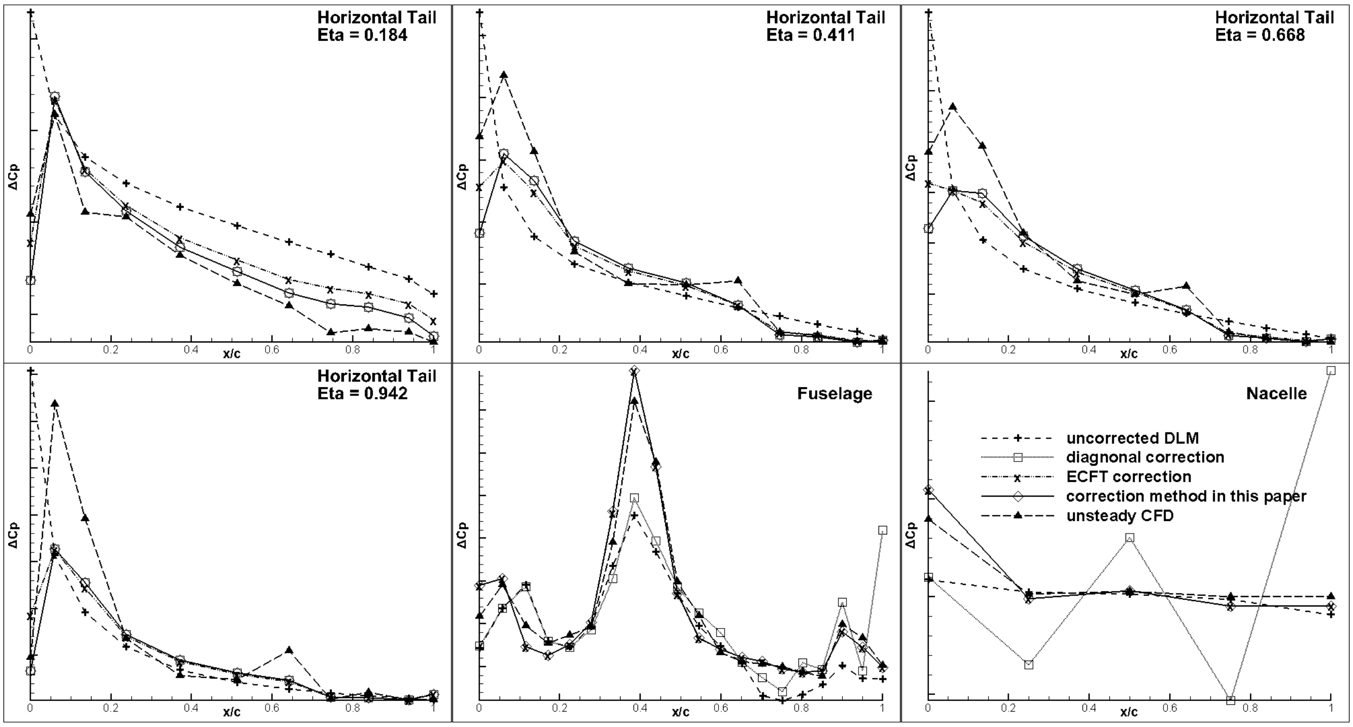

Figure 5. Real ΔCp of horizontal tail, fuselage, and nacelle component at 1 HZ.

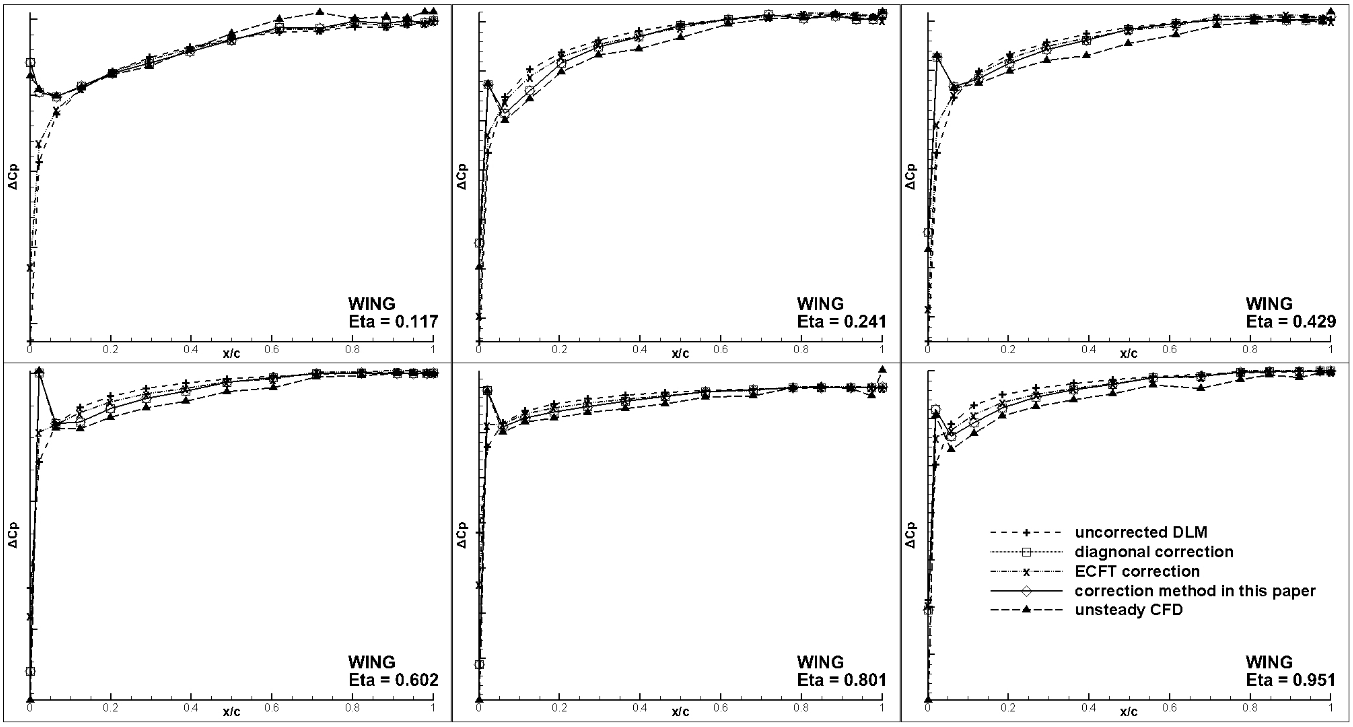

Figure 6. Imaginary ΔCp of wing component at 1 HZ.

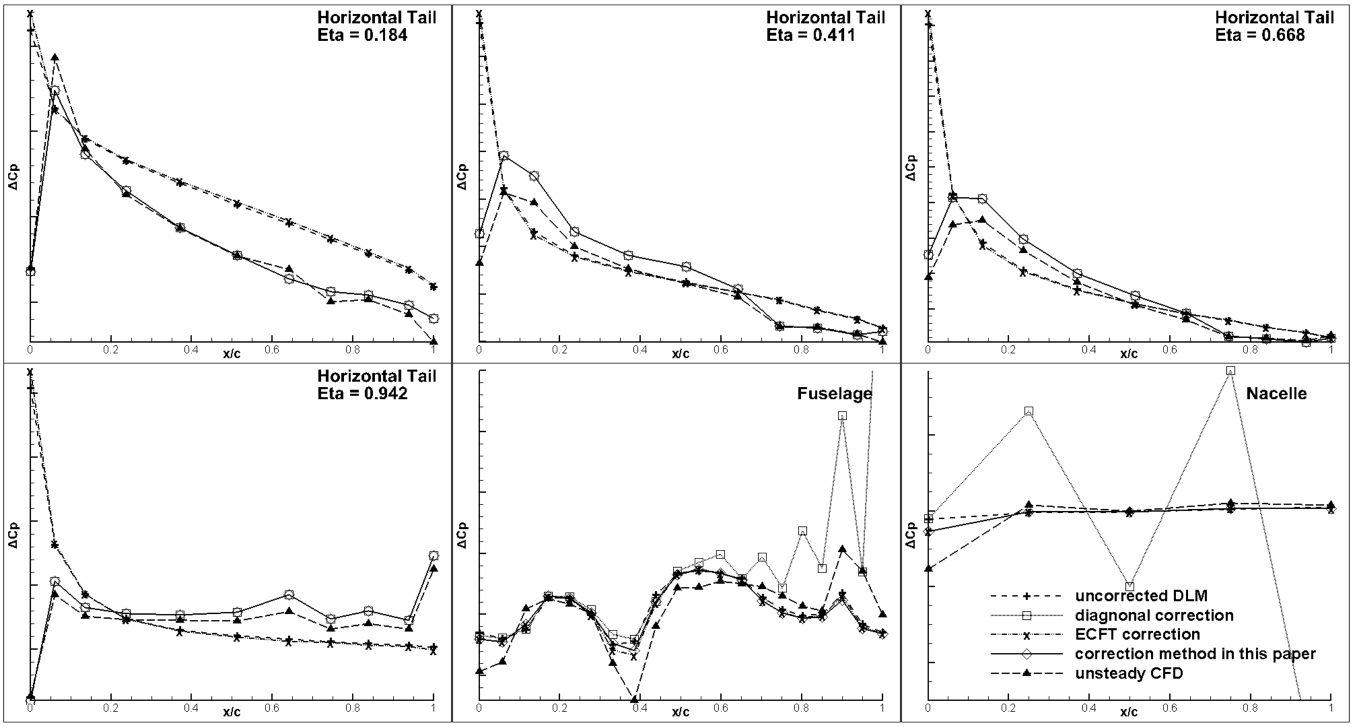

Figure 7. Imaginary ΔCp of horizontal tail, fuselage, and nacelle component at 1 HZ.

The meaning of ΔCp for lifting boxes and for body elements is shown as follows:

$$\begin{array}{l} \Delta Cp = F/(S \cdot Q) \quad \text{for lifting box} \\ \Delta Cp = F/(L \cdot Q) \text{ for body element} \end{array} \tag{27}$$

where Q represents the dynamic pressure, F denotes the force in each lifting box or each body element, S stands for the lifting box area, and L is the body element length. For the

CFD result, F represents the upper- and lower-surface force differences after mapping onto the lifting box or body element.

Comparing the real ΔCp of the wing component at 1 HZ, as shown in Figure 4, the results obtained by the diagonal correction method, ECFT correction method and the correction method proposed in this paper can all fit quite well with the unsteady CFD results. These three methods had significant advantages over the uncorrected DLM method. For the real ΔCp of the wing component, the real part of downwashes w will play a significant dominant role. This explained the excellent results obtained from all correction methods.

Comparing real ΔCp of the horizontal tail, fuselage, and nacelle component at 1 HZ, as shown in Figure 5, for the horizontal tail component, the imaginary part of downwashes w also plays a fairly important role. This contributes to the differences between all the correction methods, and the unsteady CFD results are larger than those of the wing component in Figure 4. Due to this reason, the differences between diagonal correction and ECFT correction methods also become more significant. Results obtained by the correction method proposed in this paper are consistent with the diagonal method, and slightly better than the ECFT method. Importantly, all three correction methods outperform the uncorrected DLM method. For the fuselage component and nacelle component, the diagonal correction method yields unreasonable results. Compared with the uncorrected method, both the ECFT correction method and the correction method proposed in this paper fit the unsteady CFD data quite well.

As shown in Figures 6 and 7, for the imaginary part, results obtained through the ECFT correction method are close to those received by the uncorrected DLM method, which has lost efficiency for correction purposes. For lifting surfaces of the wing component and horizontal tail component, both the diagonal correction method and the correction method proposed in this paper can fit unsteady CFD data well. However, for body elements of the fuselage component and nacelle component, the diagonal correction method obtained notably unreasonable results. In contrast, the uncorrected DLM method, ECFT method and the method proposed in this paper are relatively close to the unsteady CFD results.

To quantitatively analyze the accuracy of the various correction methods, ΔCp at each section has been summed and the dimensionless transformation carried out, as shown in Figures 8 and 9; the meaning of $\Delta Cp'$ in the figures is as follows:

$$\begin{aligned} \Delta Cp' &= \sum_{i=1}^{n} \Delta Cp \cdot c/c_{ref} \ \text{ for lifting box} \\ \Delta Cp' &= \sum_{i=1}^{n} \Delta Cp \cdot L/S_{ref} \text{ for body element} \end{aligned} \tag{28}$$

where ΔCp is the parameter in Formula (27), c is the length of every lifting box, L is the length of the body element, c_{ref} is the referenced chord length of the airplane, and S_{ref} is the referenced area of the airplane. No matter whether it is the real part or imaginary part, the correction method proposed in this paper can obtain spanwise $\Delta Cp'$ distribution results similar to CFD simulation results. Furthermore, the absolute error is small. Notably, the correction method proposed in this paper has a better performance compared to the uncorrected DLM method, the diagonal correction method, and the ECFT correction method for unsteady aerodynamic correction at 1 HZ.

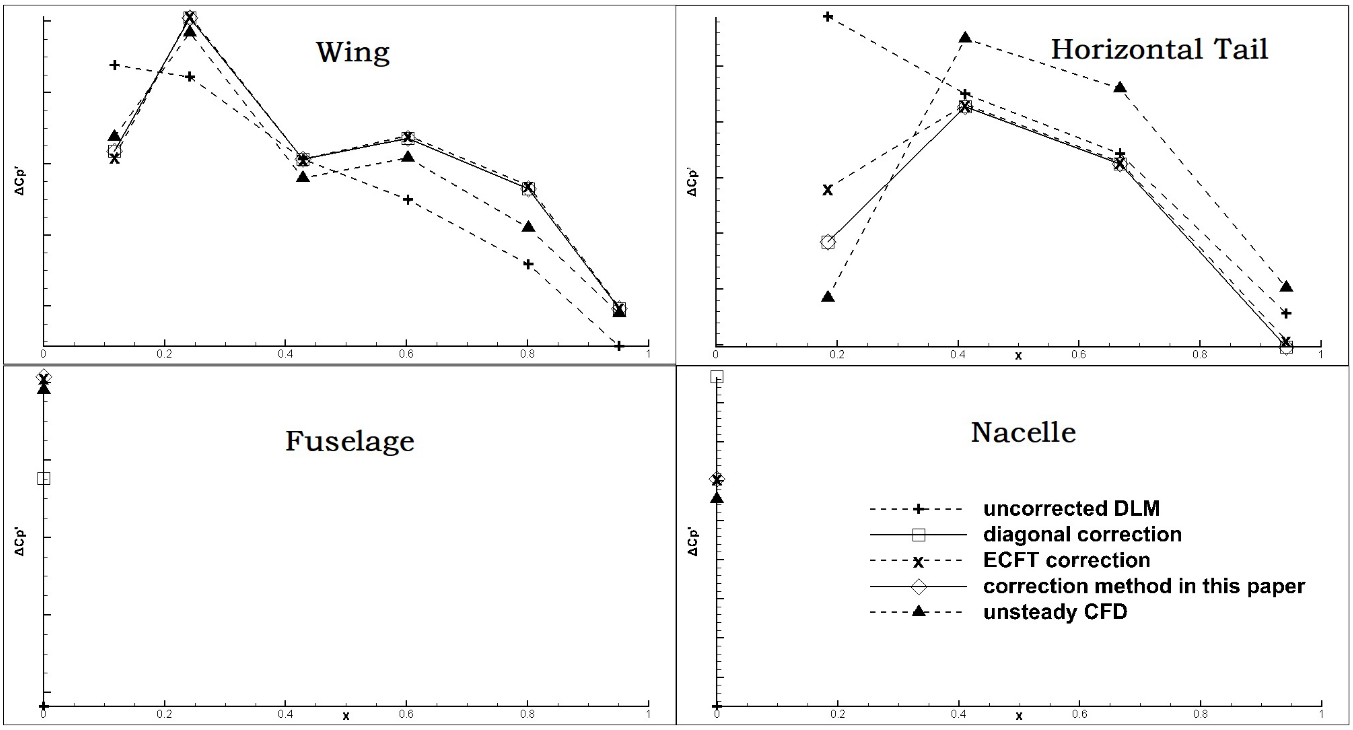

Figure 8. Real $\Delta Cp'$ of wing, horizontal tail, fuselage, and nacelle component at 1 HZ.

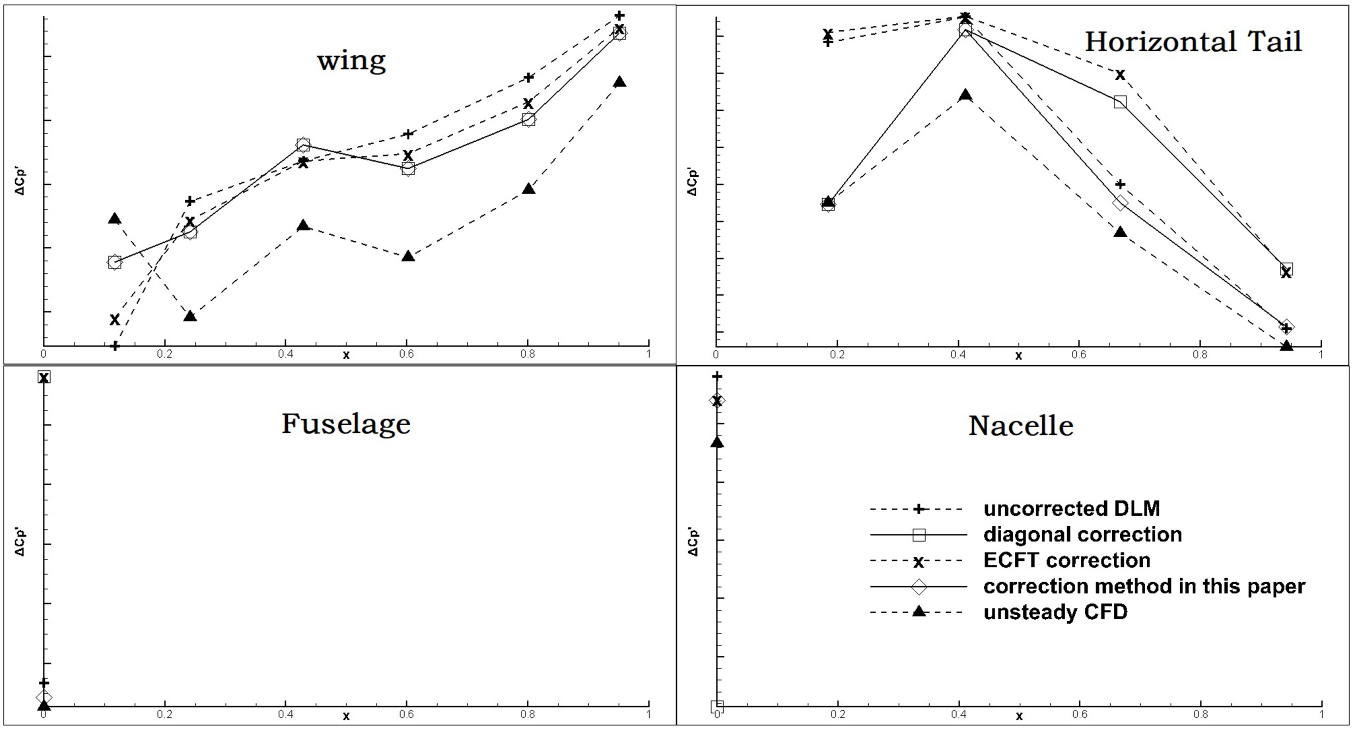

Figure 9. Imaginary $\Delta Cp'$ of wing, horizontal tail, fuselage, and nacelle component at 1 HZ.

3.2. Pressure Difference Distribution Comparison at 5 HZ

The pressure difference distributions caused by oscillation at a unit angle of attack at 5 HZ obtained by various correction methods compared to the unsteady CFD results are shown in Figures 10–13.

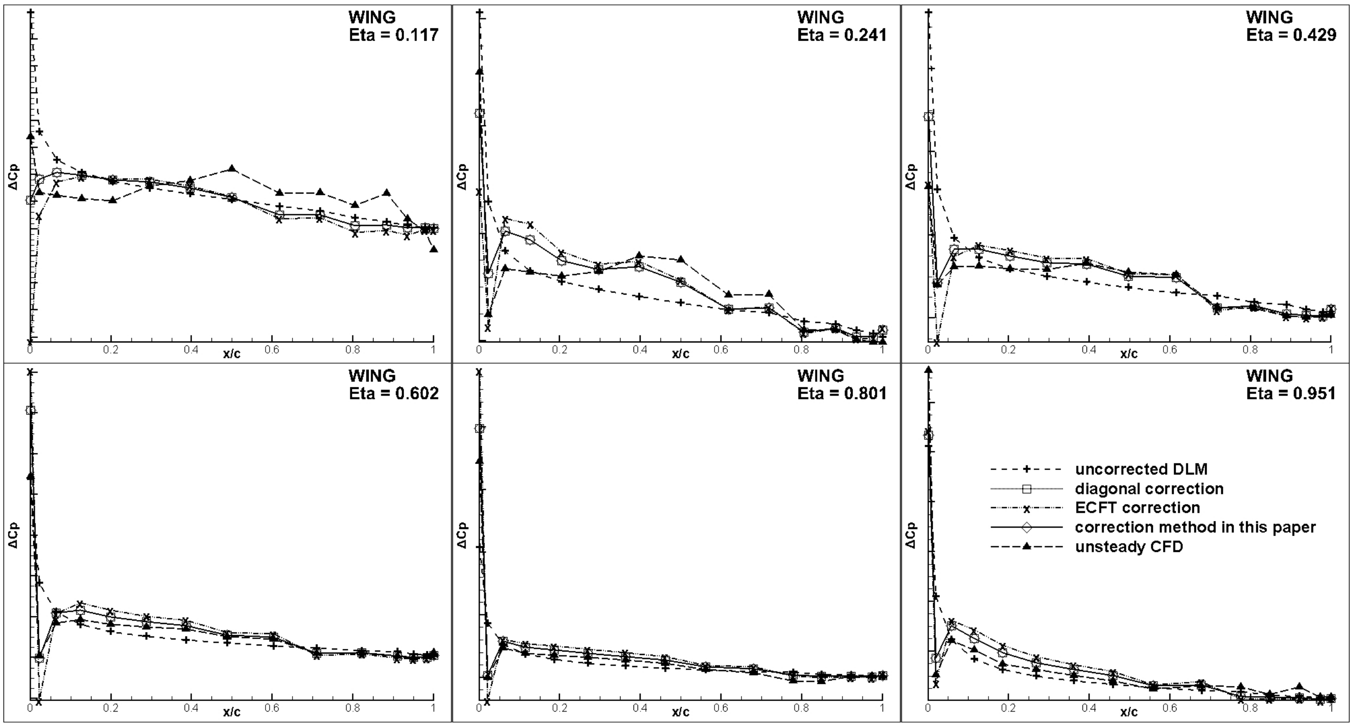

Figure 10. Real ΔCp of Wing Component at 5 HZ.

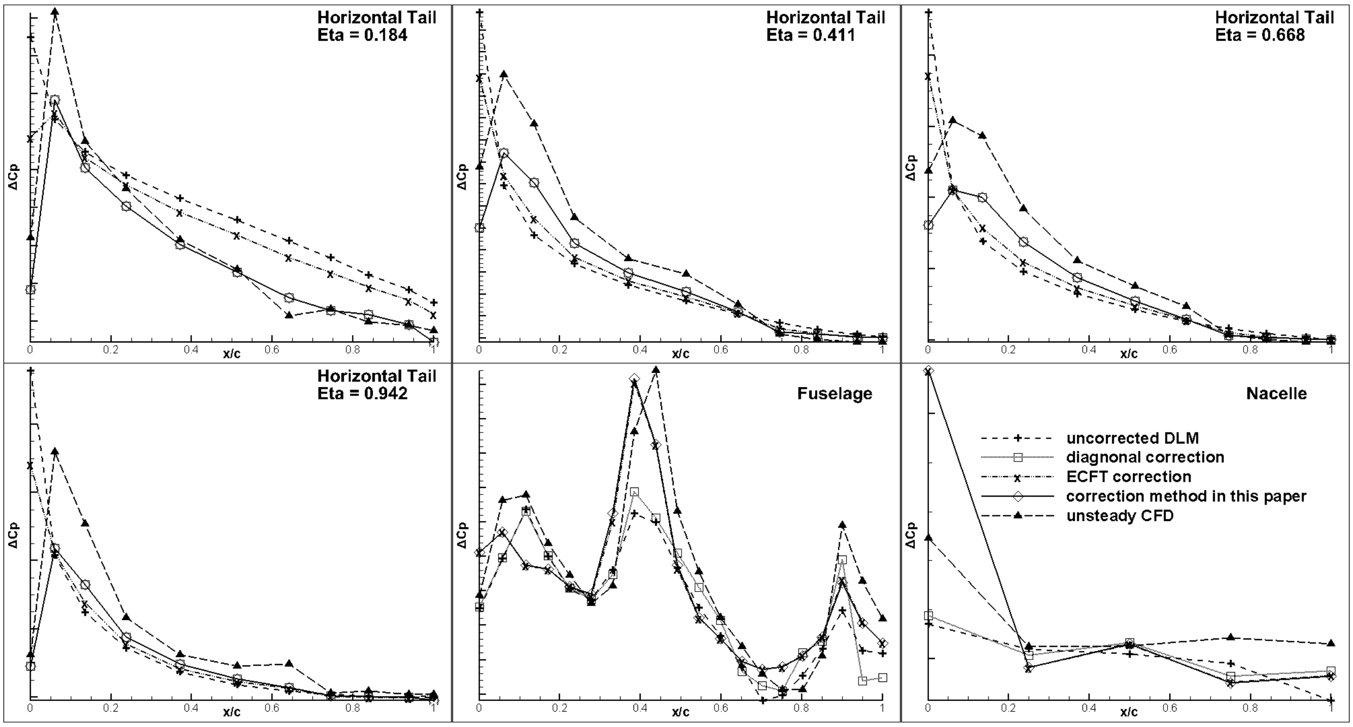

Figure 11. Real ΔCp of horizontal tail, fuselage, and nacelle component at 5 HZ.

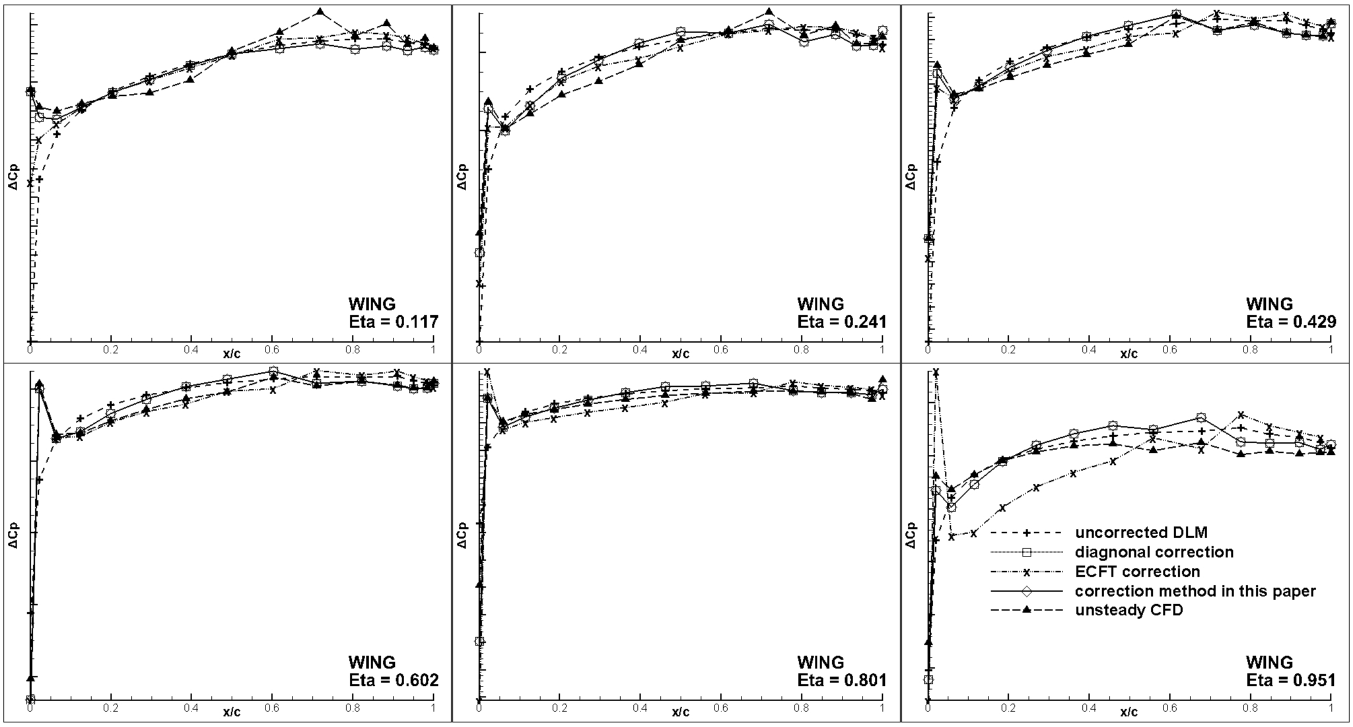

Figure 12. Imaginary ΔCp of Wing Component at 5 HZ.

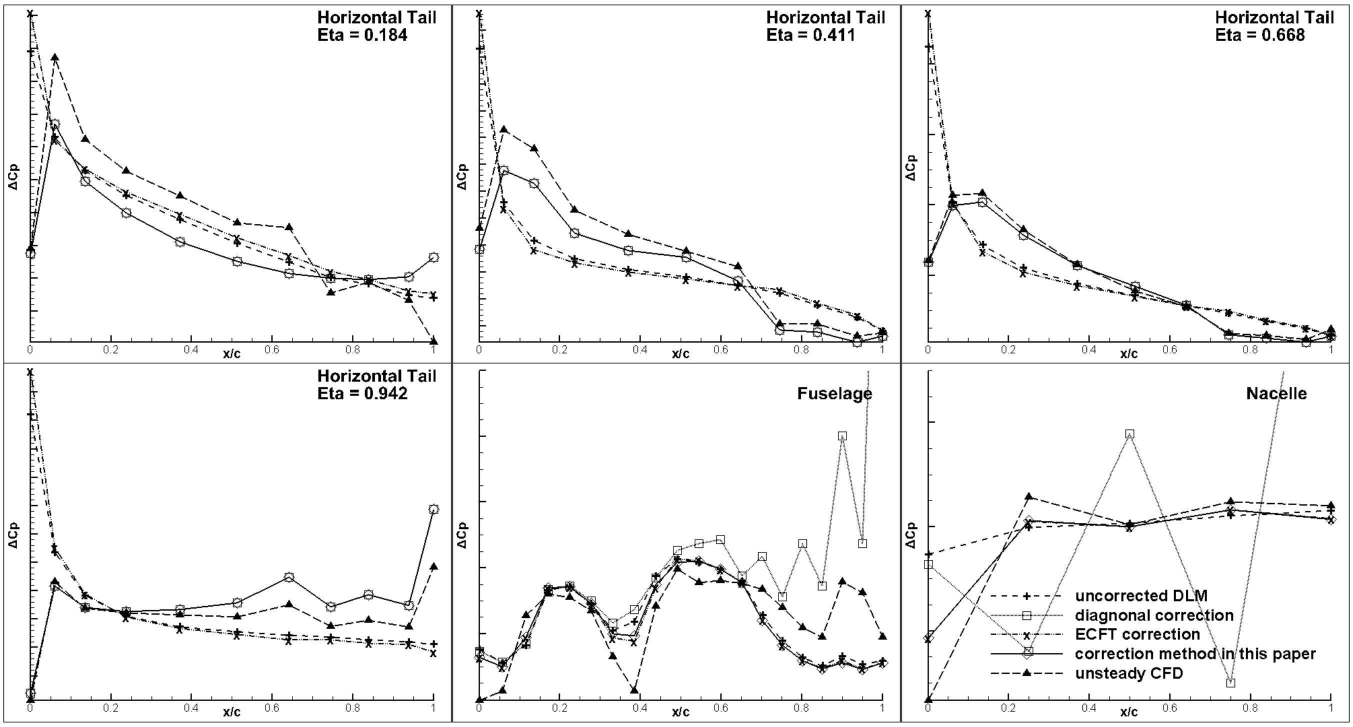

Figure 13. Imaginary ΔCp of horizontal tail, fuselage, and nacelle component at 5 HZ.

Comparing the real ΔCp of the wing component at 5 HZ, as shown in Figure 10, the effect of the correction is somewhat weakened compared to the 1 HZ case, especially for the first two sections. The reduction of the correction effect is due to the imaginary part of downwashes w playing a fairly important role. However, the effect on the other four profiles is still good, and compared to the uncorrected DLM method, the correction still achieves a certain good effect.

Comparing real ΔCp of the horizontal tail, fuselage, and nacelle component at 5 HZ, as shown in Figure 11, for the horizontal tail component, the imaginary part of downwashes w will play an important role. The null space of the real part of downwashes w results in the ECFT correction method being close to the uncorrected DLM method. For the horizontal tail, both the diagonal correction method and the correction method proposed in this paper have obtained relatively good results. For the body elements, especially for the fuselage, both the ECFT method and the method in this paper have obtained relatively good results.

For the imaginary part, as shown in Figures 12 and 13, the results are largely consistent with the real part in Figures 10 and 11. For wing components, horizontal tail components, fuselage or nacelle, the correction method proposed in this paper achieves a certain good effect.

The real part and imaginary part of $\Delta Cp'$ are shown in Figures 14 and 15; the spanwise $\Delta Cp'$ distribution results obtained by the correction method proposed in this paper are similar to the CFD results, but the advantage is not as pronounced when compared with the uncorrected DLM method for the imaginary part of the horizontal tail.

3.3. Pressure Difference Distribution Comparison at 10 HZ

The pressure difference distributions caused by oscillation at a unit angle of attack at 10 HZ obtained by different correction methods compared with the unsteady CFD results are shown in Figures 16–19. The real part and imaginary part of $\Delta Cp'$ are shown in Figures 20 and 21. Compared to the uncorrected DLM, the diagonal correction method and the ECFT correction method, the correction method described in this paper still has certain advantages. However, the difference with unsteady CFD has been gradually expanded, especially for the real $\Delta Cp'$ of the horizontal tail component in Figure 20 and the imaginary $\Delta Cp'$ of the wing component in Figure 21. The absolute error of the correction method described in this paper is unacceptable.

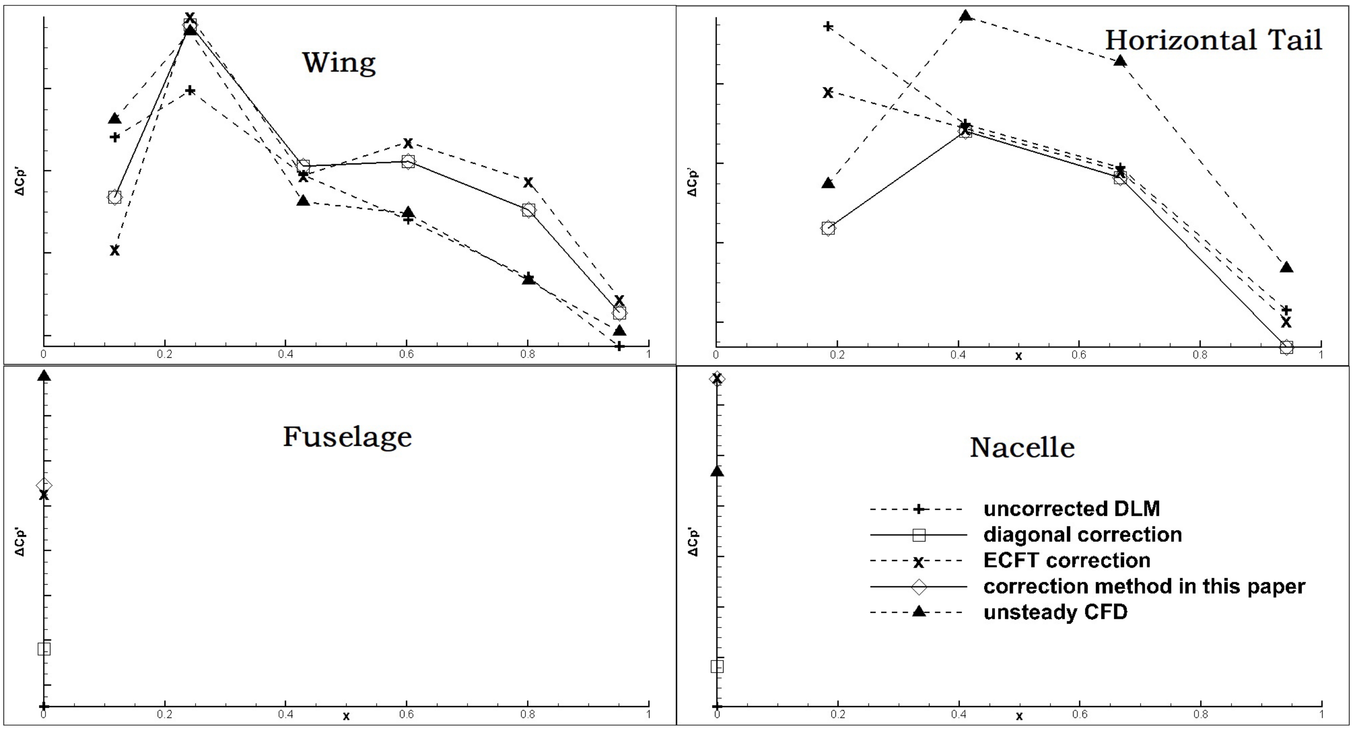

Figure 14. Real $\Delta Cp'$ of wing, horizontal tail, fuselage, and nacelle component at 5 HZ.

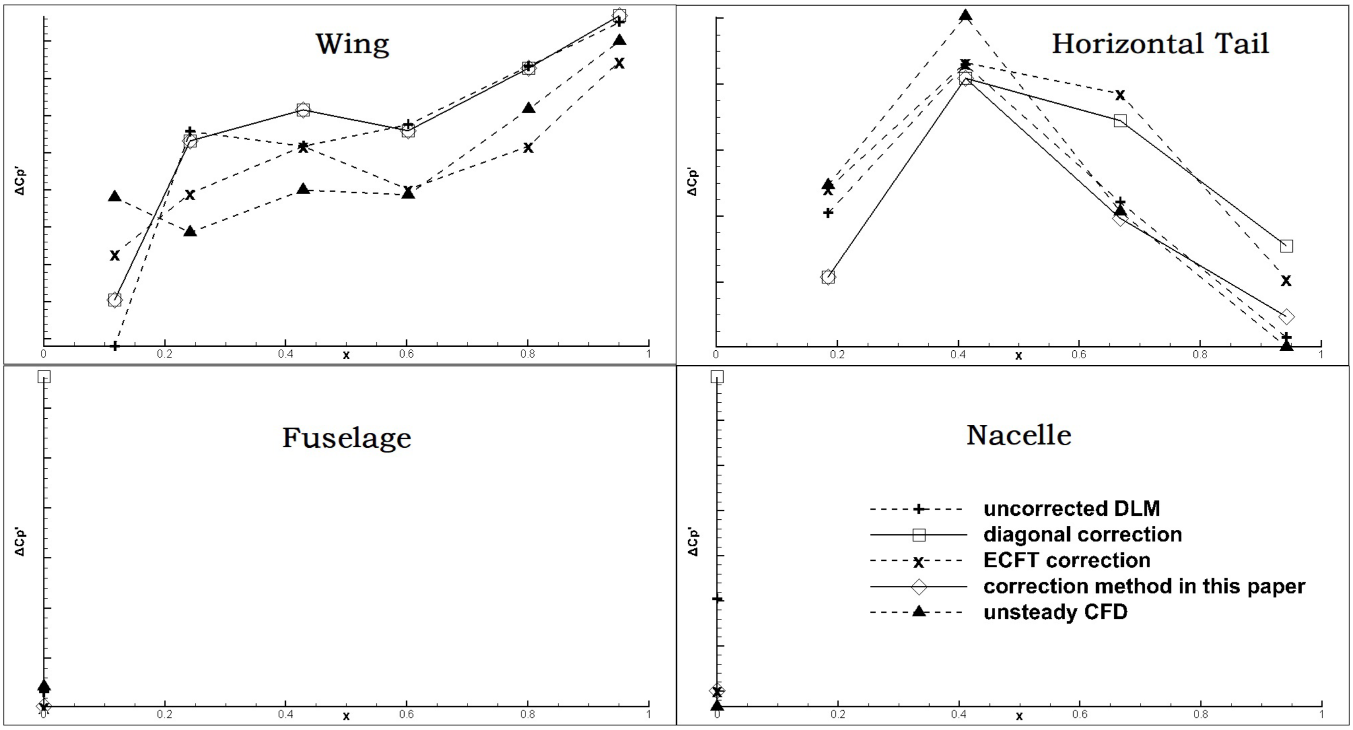

Figure 15. Imaginary $\Delta Cp'$ of wing, horizontal tail, fuselage, and nacelle component at 5 HZ.

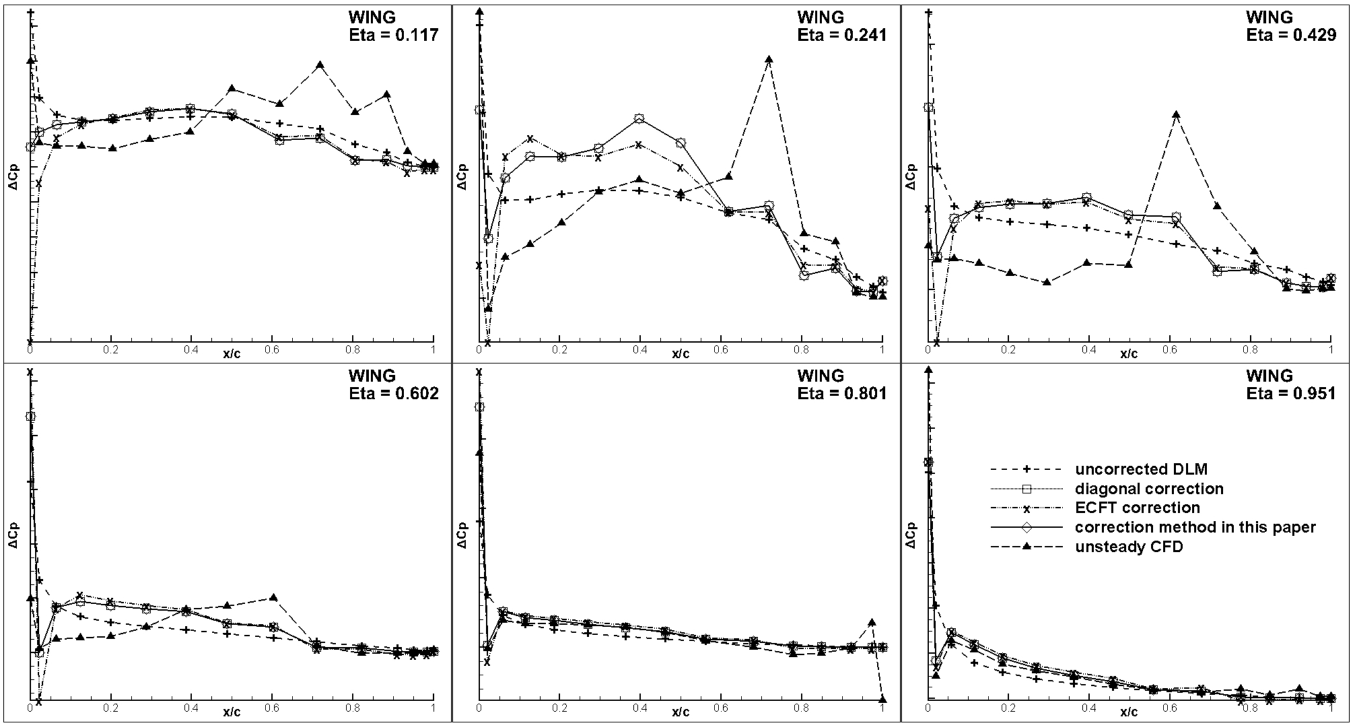

Figure 16. Real ΔCp of Wing Component at 10 HZ.

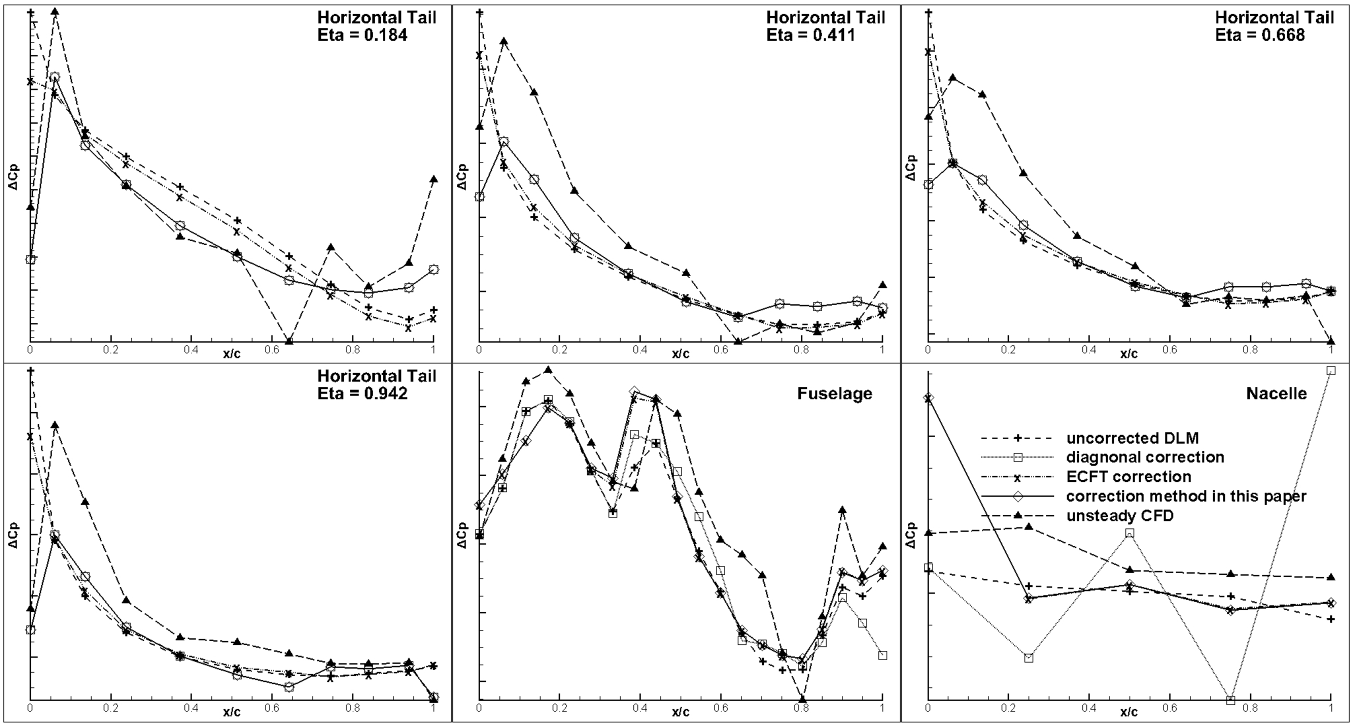

Figure 17. Real ΔCp of horizontal tail, fuselage, and nacelle component at 10 HZ.

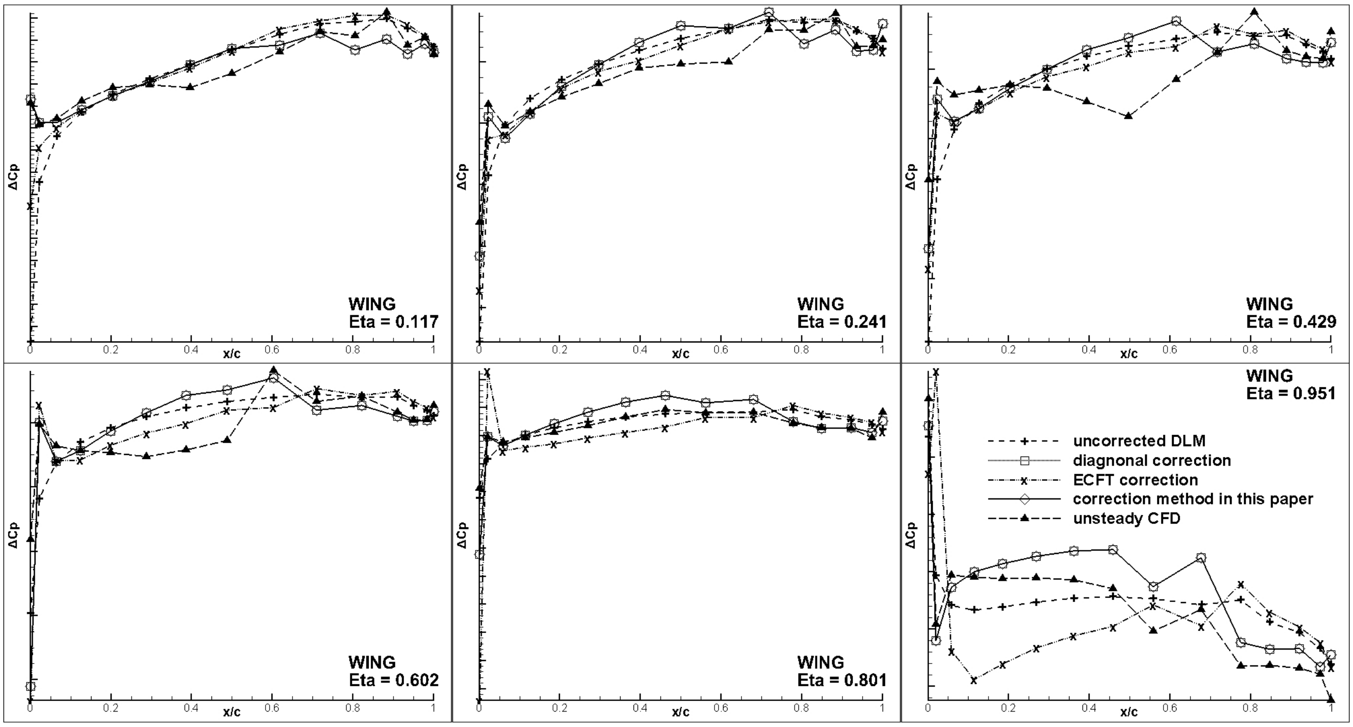

Figure 18. Imaginary ΔCp of Wing Component at 10 HZ.

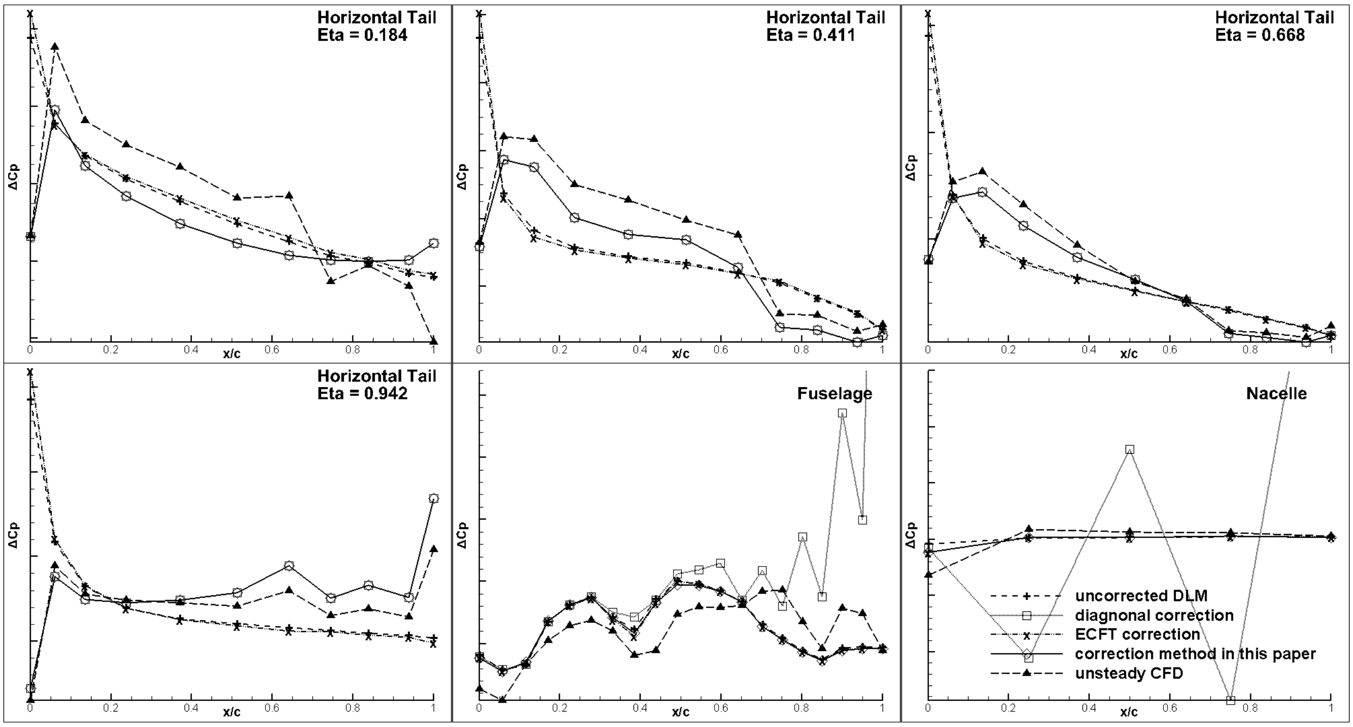

Figure 19. Imaginary ΔCp of horizontal tail, fuselage, and nacelle component at 10 HZ.

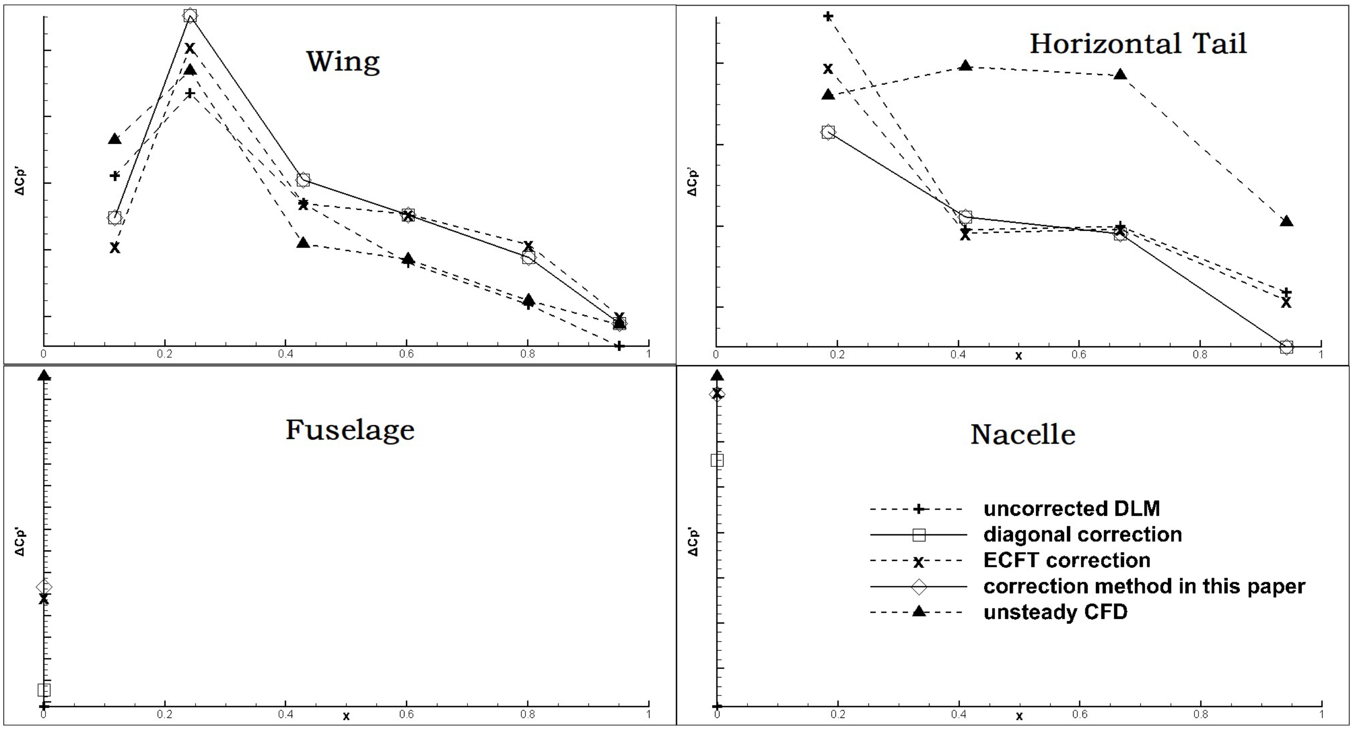

Figure 20. Real $\Delta Cp'$ of wing, horizontal tail, fuselage, and nacelle component at 10 HZ.

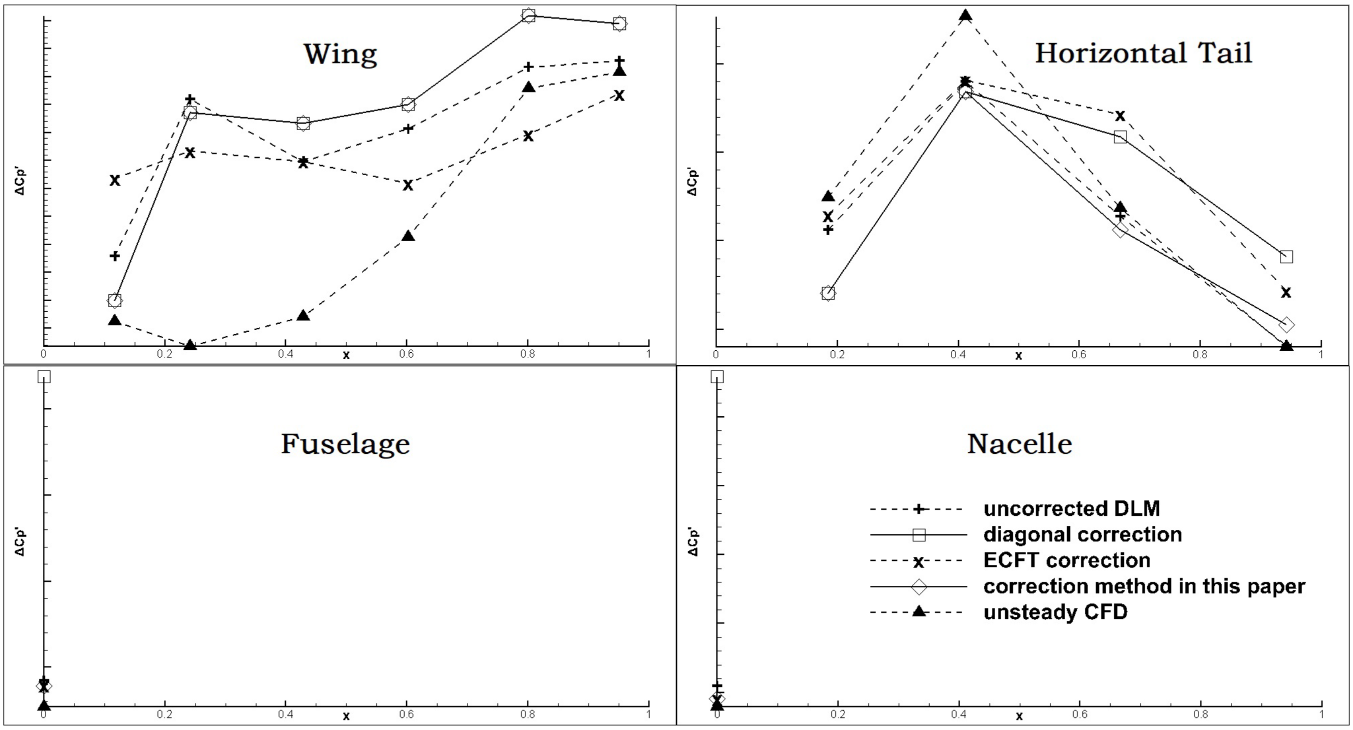

Figure 21. Imaginary $\Delta Cp'$ of wing, horizontal tail, fuselage, and nacelle component at 10 HZ.

3.4. Pressure Difference Distribution Comparison at 20 HZ

The pressure difference distributions caused by oscillation at a unit angle of attack at 20 HZ obtained by different correction methods compared with the unsteady CFD results are shown in Figures 22–25. The real part and imaginary part of $\Delta Cp'$ are shown in Figures 26 and 27. The error between unsteady CFD and any other correction method or uncorrected DLM is quite significant, and is unacceptable.

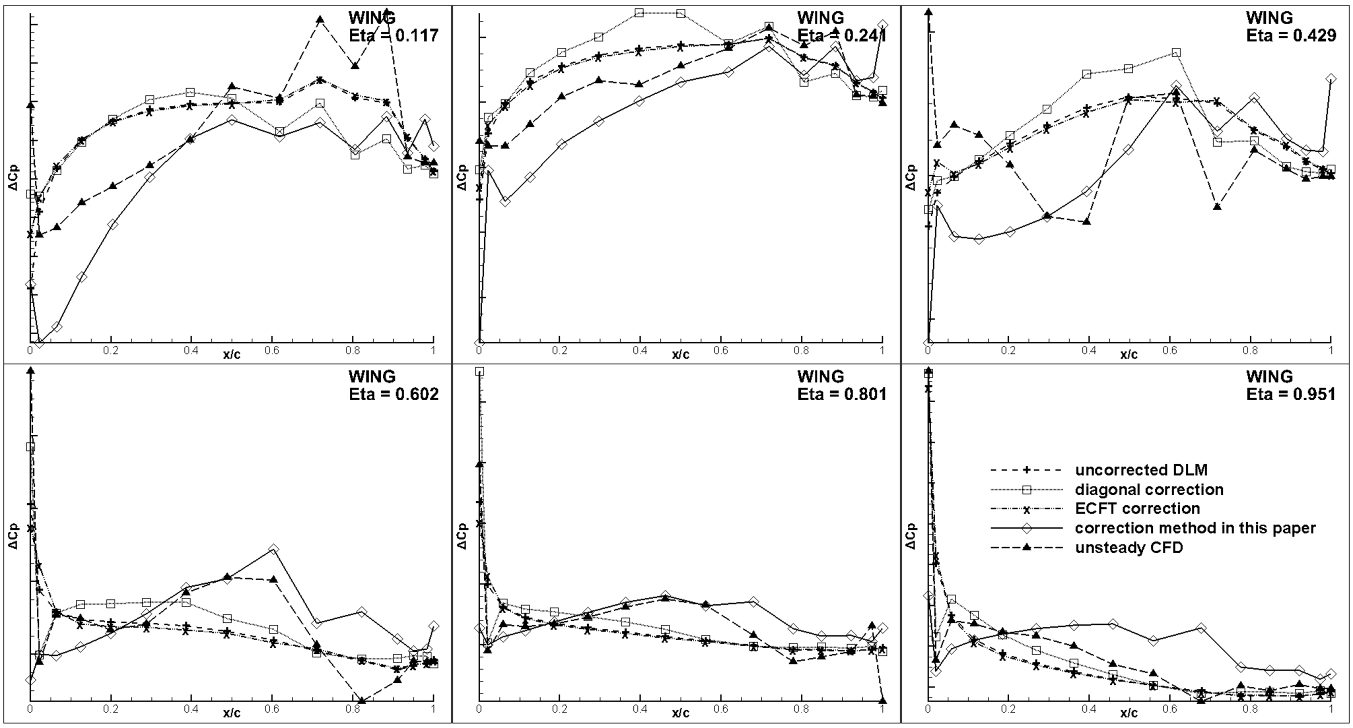

Figure 22. Real ΔCp of Wing Component at 20 HZ.

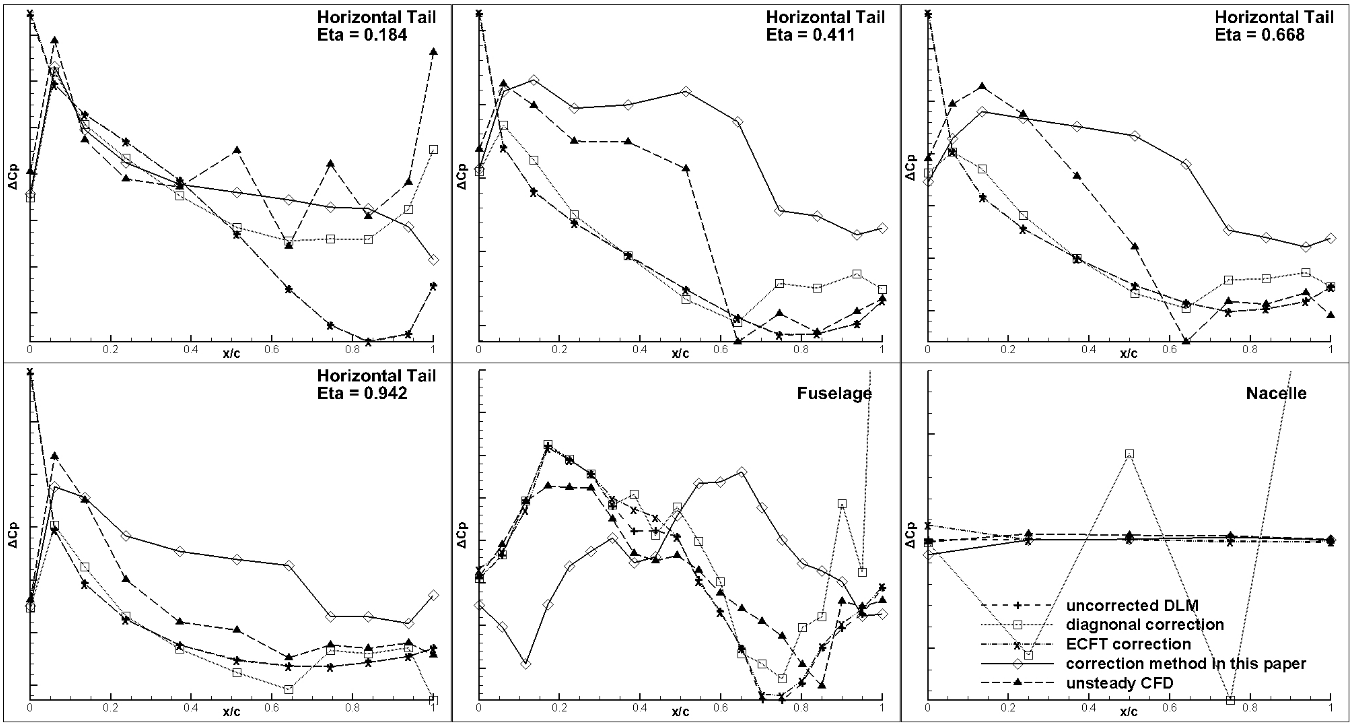

Figure 23. Real ΔCp of horizontal tail, fuselage, and nacelle component at 20 HZ.

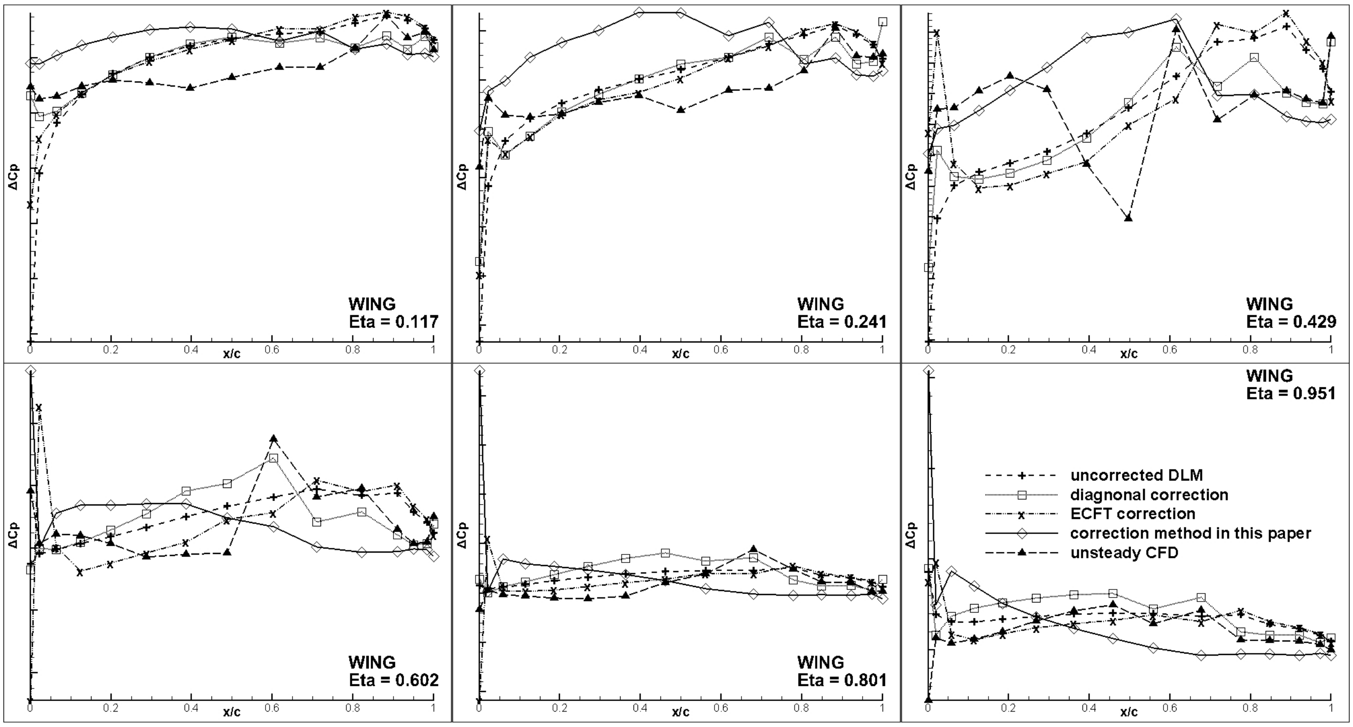

Figure 24. Imaginary ΔCp of Wing Component at 20 HZ.

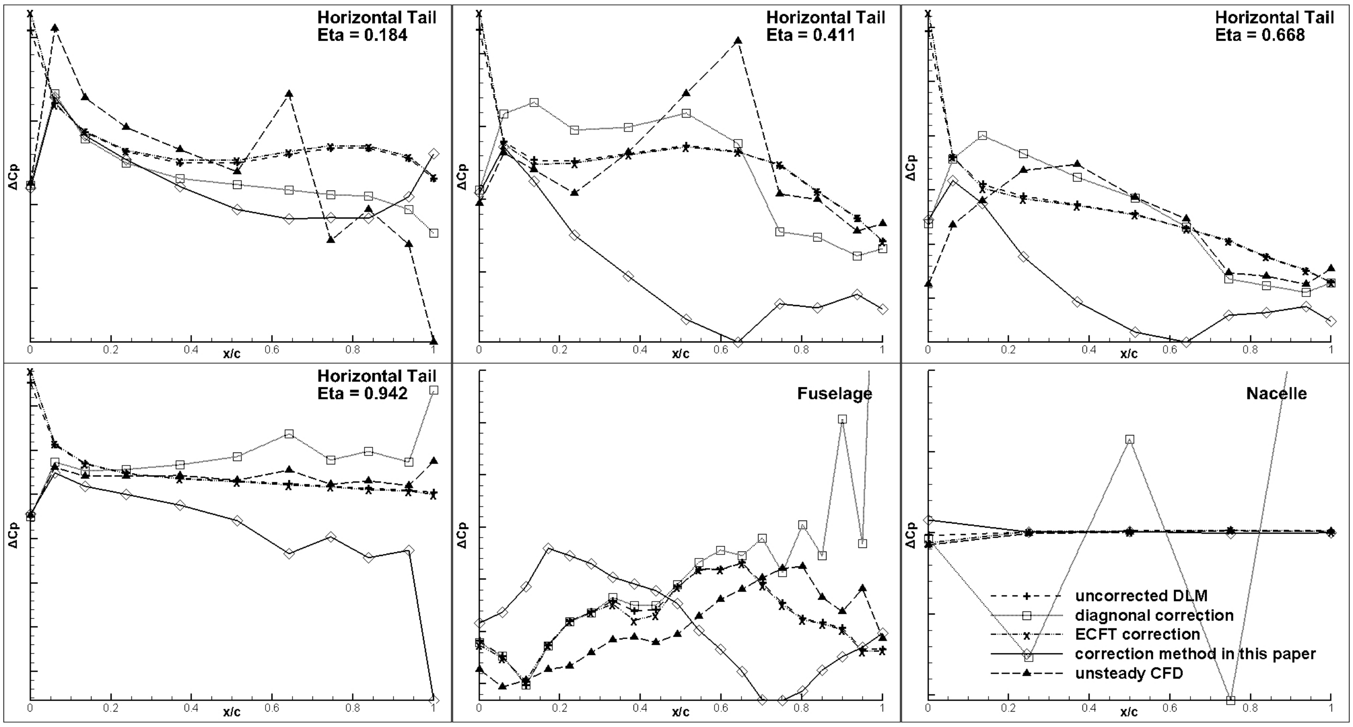

Figure 25. Imaginary ΔCp of horizontal tail, fuselage, and nacelle component at 20 HZ.

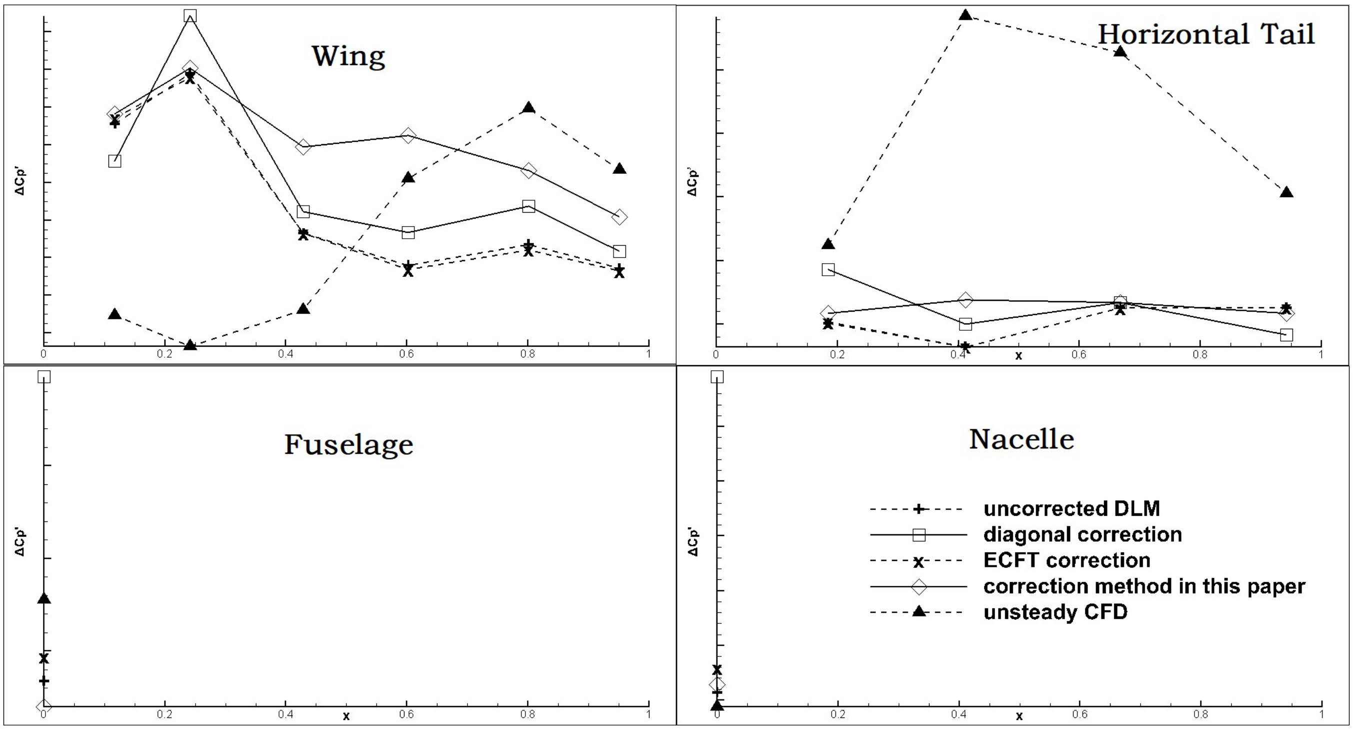

Figure 26. Real $\Delta Cp'$ of wing, horizontal tail, fuselage, and nacelle component at 20 HZ.

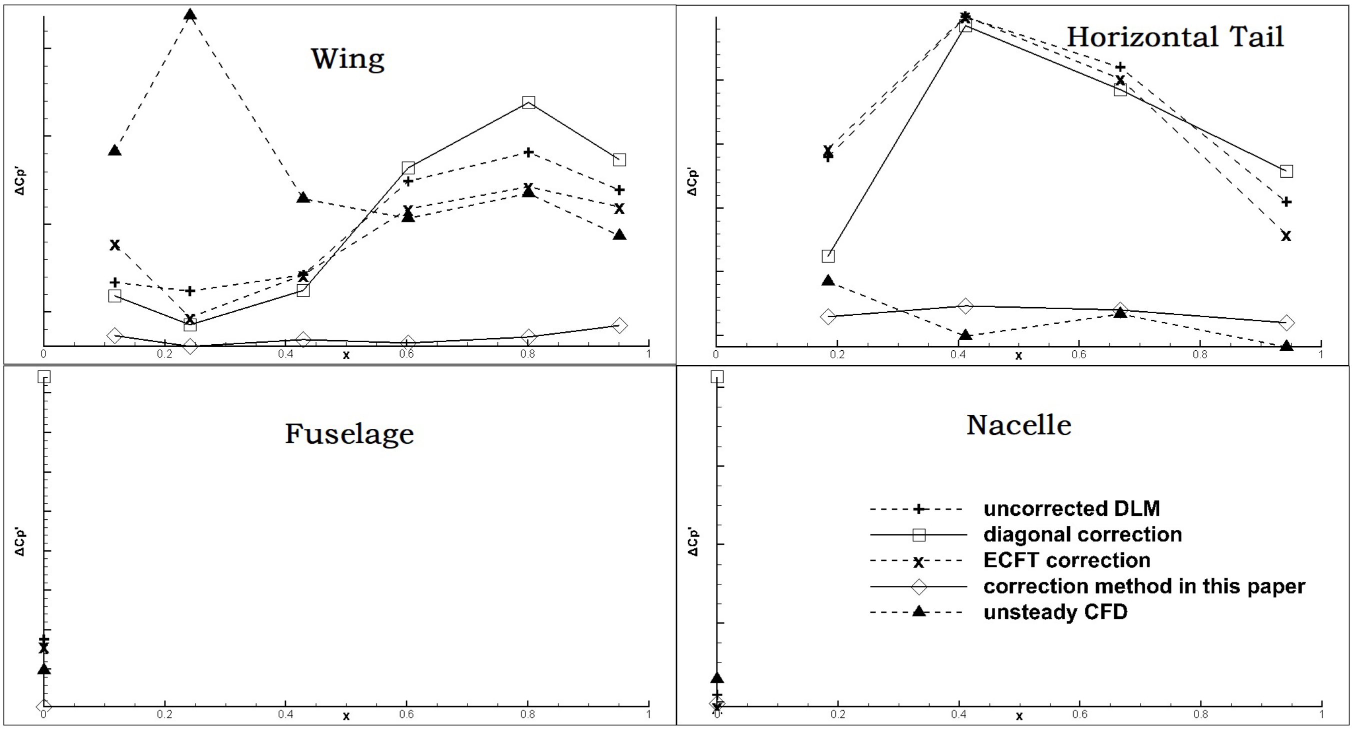

Figure 27. Imaginary $\Delta Cp'$ of wing, horizontal tail, fuselage, and nacelle component at 20 HZ.

4. Discussion

In theory, due to the use of steady aerodynamics for correction, for the real part of unsteady aerodynamics, the smaller the frequency, the closer the real part of $[AIC]$ to a static situation $k = 0$, and the smaller the imaginary part of w, the more accurate the correction results will be. That is the reason why the results for small frequency are better, and the results for the wing component are better than those for the horizontal tail component.

The diagonal correction method has a more physical meaning, and represents the factor for each element; hence even for the imaginary part of unsteady aerodynamics, the agreement between the correction method and unsteady CFD is also good. The correction method in this paper inherits this advantage and has been further improved and extended. However, unlike the real part results, for the imaginary part, in the same frequency, the larger the imaginary part of w, the more accurate the correction results will be. The imaginary parts of unsteady aerodynamics are composed of the real part of $[AIC]$ multiplied by the imaginary part of w, and the imaginary part of $[AIC]$ multiplied by the real part of w. When the imaginary part of w is larger than the real part, the real part of $[AIC]$ will be dominant. That is why in Figures 9, 15, 21 and 27, the results for the horizontal tail component after the correction method in this paper are better than those for the wing component.

5. Conclusions

The present diagonal correction method or ECFT method are both unsuitable for an unsteady subsonic wing–body interference model. In this paper, the diagonal correction method and ECFT method are extended to the wing–body interference model directly, but there have been varying degrees of problems in analyzing unsteady wing–body aerodynamics. Combining the advantages and disadvantages of the diagonal correction method and the ECFT method, a correction method for the unsteady subsonic wing–body interference model is proposed. In comparison to the uncorrected DLM, the diagonal correction method, and the ECFT method, the results of different aircraft components obtained through the simulation of a transonic passenger aircraft show a better consistency with the results from the unsteady CFD simulations. When the frequency of unsteady motion is smaller than

5 HZ, the correction method in this paper can obtain certain benefits in terms of accuracy, not only for the lifting boxes but also for the body elements. This correction method can be used to obtain more accurate unsteady aerodynamics in low-frequency modes, and improve the precision of rigid–elastic coupling analysis.

Author Contributions: Methodology, K.M.; conceptualization, W.J.; project administration, M.Z.; validation, H.Z. All authors have read and agreed to the published version of the manuscript.

Funding: This research received no external funding.

Data Availability Statement: Not applicable.

Conflicts of Interest: The authors declare no conflict of interest. The funders had no role in the design of the study; in the collection, analyses, or interpretation of data; in the writing of the manuscript; or in the decision to publish the results.

References

1. Robert, C.S.; John, J.C.; Maxwell, B. Dynamic Modeling Uncertainty Affecting Control System Design. AIAA Paper, No. 84-1057. In Proceedings of the 25th Structures, Structural Dynamics and Materials Conference, Palm Springs, CA, USA, 14–16 May 1984.
2. Martin, R.W.; David, K.S. Flight Dynamics of Aeroelastic Vehicles. *J. Aircr.* **1988**, *25*, 563–571.
3. Saltari, F.; Riso, C.; Matteis, G.D.; Mastroddi, F. Finite-Element-Based Modeling for Flight Dynamics and Aeroelasticity of Flexible Aircraft. *J. Aircr.* **2017**, *54*, 2350–2366. [CrossRef]
4. Castells Marin, P.; Poetsch, C. Simulation of Flexible Aircraft Response to Gust and Turbulence for Flight Dynamics Investigations. *AIAA SciTech Forum.* 2020.
5. Lee-Rausch, E.M.; Batina, J.T. Wing Flutter Computations Using an Aerodynamic Model Based on the Navier-Stokes Equations. *J. Aircr.* **1996**, *33*, 1139–1147. [CrossRef]
6. Dumlupinar, E.; Murthy, V.R. CFD Studies of Unsteady Compressible Effects on Airfoils and Ramping Motion. In Proceedings of the 29th AIAA Applied Aerodynamics Conference, Honolulu, HI, USA, 27–30 June 2011.
7. Albano, E.; Rodden, W.P. A Doublet-Lattice Method for Calculating Lift Distribution on Oscillating Surfaces in Subsonic Flows. *AIAA J.* **1968**, *7*, 279–285. [CrossRef]
8. Giesing, J.P.; Kalman, T.P.; Rodden, W.P. Subsonic Unsteady Aerodynamics for General Configurations. AIAA Paper, No. 72-26. In Proceedings of the 10th Aerospace Sciences Meeting, San Diego, CA, USA, 17–19 January 1972.
9. Baker, M.L.; Yuan, K.; Goggin, P.J. Calculation of Corrections to Linear Aerodynamic Methods for Static and Dynamic Analysis and Design. In Proceedings of the 39th AIAA/ASME/ASCE/AHS/ASC Structures, Structural Dynamics, and Materials Conference and Exhibit, Long Beach, CA, USA, 20–23 April 1998; pp. 3100–3110.
10. Giesing, J.P.; Kalman, T.P.; Rodden, W.P. *Correction Factor Techniques for Improving Aerodynamic Prediction Methods*; NASA CR-144967; National Aeronautics and Space Administration: Washington, DC, USA, 1976.
11. Moreno, R.; Narisetti, R.; von Knoblauch, F.; Taylor, P.F. A Modification to the Enhanced Correction Factor Technique to Correlate with Experimental Data. In Proceedings of the 56th AIAA/ASCE/AHS/ASC Structures, Structural Dynamics, and Materials Conference, Kissimmee, FL, USA, 5–9 January 2015; pp. 1–17.
12. Jadic, I.; Hartley, D.; Giri, J. An Enhanced Correction Factor Technique for Aerodynamic Influence Coefficient Method. In Proceedings of the MSC's 1999 Aerospace User's Conference, Long Beach, CA, USA, 7–11 June 1999.
13. Mao, K.; Jing, W.; Cheng, P.; Liu, X.; Sun, Y.; Zhang, M. A Modification to the Enhanced Correction Factor Technique for the Subsonic Wing-Body Interference Model. *Aerospace* **2023**, *10*, 40. [CrossRef]
14. Lacombe, F.; Pelletier, D.; Garon, A. Compatible wall functions and adaptive remeshing for the k-ω SST model. In Proceedings of the AIAA SciTech Forum, San Diego, CA, USA, 7–11 January 2019.